

Microwave plasma-activated chemical vapour deposition of diamond: an investigation into N- containing plasmas



By Mack Johnson

University of Bristol
School of Chemistry
Faculty of Science

First assessor: Professor Mike Ashfold
Second assessor: Professor Paul May

April 2014

A dissertation submitted to the University of Bristol in partial fulfilment
of the requirements for the Honours degree of MSci Chemical Physics.

Contents

Abstract	3
1. Review of the Literature	4
1.1 <i>Introduction to diamond, its properties and applications</i>	4
1.1.1 <i>Mechanical</i>	4
1.1.2 <i>Thermal</i>	6
1.1.3 <i>Electrical</i>	7
1.2 <i>Thin films and growth</i>	11
1.2.1 <i>Amorphous carbon phases</i>	11
1.2.2 <i>Chemical vapour deposition of diamond</i>	12
1.2.3 <i>Growth mechanism of CVD diamond</i>	17
1.2.4 <i>Thin films and characterisation</i>	22
1.3 <i>MPCVD</i>	27
1.3.1 <i>Principle of operation</i>	27
1.3.2 <i>Computational studies</i>	32
1.3.3 <i>Probing plasma characteristics</i>	35
1.3.4 <i>Motivation for study: N-containing plasmas</i>	37
2. Experimental Details	38
2.1 <i>Brief description of the project</i>	38
2.2 <i>Apparatus and measurements</i>	38
2.2.1 <i>Apparatus</i>	38
2.2.2 <i>Measurements</i>	40
2.3 <i>Using PGOPHER to fit experimental data</i>	42
3. Results	45
3.1 <i>Spatial Profiles</i>	45
3.2 <i>Microwave Power</i>	47
3.3 <i>Nitrogen atom flow</i>	49
4. Discussion	51
5. Conclusion	53
6. Suggestions for further work	54

7. Acknowledgements.....	55
8. References.....	56

Abstract

Diamond is a remarkable material, exhibiting unparalleled mechanical, thermal and electrical properties that will see use in many different applications including coatings and electronic devices, motivating the desire to grow high quality synthetic diamond. This project started by reviewing the present literature on the microwave-plasma activated chemical vapour deposition (MPCVD) of diamond and found that the addition of N_2 to the precursor gas mixture increased the diamond growth rate by over a factor of two on all substrate orientations. This finding motivated the study of N-containing plasmas. Plasmas consisting of N_2/H_2 and NH_3/H_2 were studied using optical emission spectroscopy (OES). OES measurements were taken for variation of the microwave power, nitrogen atom flow and spatial profile coordinate z for both plasmas. The experimental OES data was then simulated using PGOPHER in order to calculate quantities such as the N_2 , NH emission intensities and the gas temperature. Significant results in this study found that the N_2 emission was greater in an NH_3 plasma than that of N_2 at the core of the plasma. In addition, the gas temperature was constant for an NH_3 plasma whereas in an N_2 plasma there was a linear increase as a function of microwave power. The results from this work may be input into a computational model of an MPCVD process in order to understand deeper aspects of the plasma chemistry that may not necessarily be accessible experimentally. This work highlights the fidelity of PGOPHER as a simulation tool and OES for probing plasma characteristics.

Review of the Literature

1.1 *Introduction to diamond, its properties and applications*

1.1.1 *Mechanical properties*

In the present times, diamond is becoming an important material in a variety of different applications. Diamond is an allotrope of carbon (C), meaning it has a different solid state crystal structure than other forms of carbon such as graphite and graphene for example. The contrast between the crystal structures of graphite and diamond is shown in Figure 1 [1, 2]. The existence of carbon's allotropes is a consequence of being able to exhibit sp^1 , sp^2 and sp^3 hybridisation from mixing of s and p orbitals. Diamond consists of covalent sp^3 hybridised C atoms forming directional σ bonds in a tetrahedral network. The lattice can be visualised as two interpenetrating face-centred cubic (fcc) lattices with a basis of atom positions at $R=0$ and $R=1/4(x,y,z)$ in units of the lattice constant a . These strong bonding interactions and the high atom density (3.515 g cm^{-3}) account for the reported hardness of 100 GPa [3] and high values for the Young's, shear and bulk moduli, represented by E , G and K respectively reported in table 1 [4]. These properties make diamond an ideal material for providing a hard protective coating to soft infrared (IR) transparent window materials such as zinc sulphide (ZnS), zinc selenide (ZnSe) and germanium (Ge) as diamond is also optically transparent in this region [5-8]. It should be noted that free-standing diamond itself can serve as an IR window for the same purposes. However, the caveat is that growing synthetic diamond from a method such as chemical vapour deposition (this will be discussed later) is slow when requiring a film thickness on the order of 1mm. In this case, free standing diamond is suited for applications in adverse conditions such as IR transparent windows for lasers that output $\geq 1 \text{ kW}$ of power, where materials like ZnSe and Ge cannot function. ZnSe possesses a high (relatively much greater than diamond) coefficient of thermal expansion. Because the material is soft and brittle, thermal shock arising from absorption of infrared heat radiation may cause it to fail *in-situ*. This therefore means that free standing diamond is suitable for applications such as optics for carbon dioxide (CO_2) lasers [9] and IR missile domes [10]. The effectiveness of diamond as a protective coating has also been utilised in biomaterial applications such as implantation surgery, where a thin film of diamond can function to reduce wear on a load-bearing joint or as a blood-contacting implant for heart valves or stents due to its biocompatibility [11-14]. Conventional materials used to produce implants are generally based on alloys of titanium (Ti), chromium (Cr) and various ceramics and polymers [15]. These materials have to compromise between their mechanical and chemical properties in an *in vitro* environment. For example, the human body fluid contains approximately 1 wt. % sodium chloride (NaCl) as well as a vast array of other ionic salts and organic compounds which can corrode the alloy through different mechanisms including pitting corrosion and chemical reactions that promote release of metal ions. The inclusion of a film of diamond

therefore acts as a passivation layer. Research from Lappalainen et al in 1998 showed a significant improvement in the corrosion resistance when coating stainless steel, Ti-6Al-4V, alumina and CoCrMo with thin films of diamond ranging from 0.2-1 μm [16]. Results from other studies also point to diamonds benefit as a biomaterial and are given in the references at the reader's interest [17-19]. A picture of a diamond ankle joint is given in figure 2.

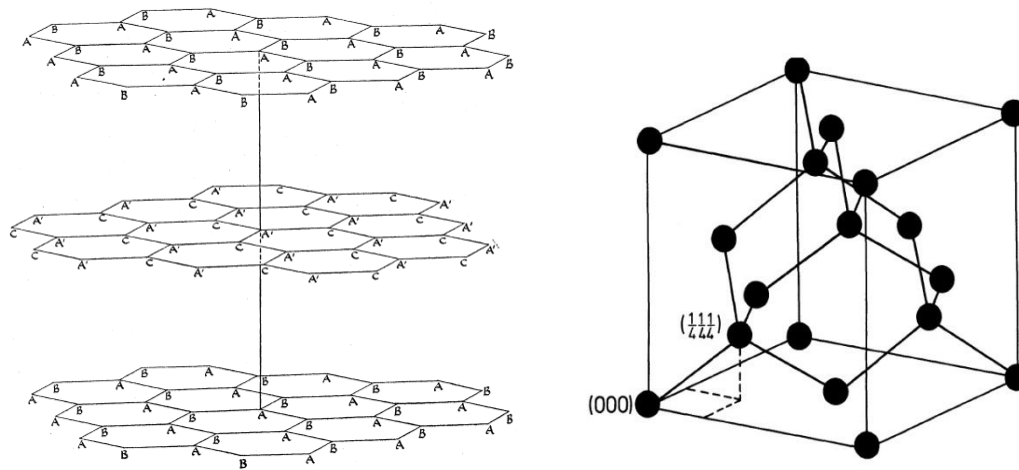


Figure 1: Crystal structures of graphite adapted from reference [1] (shown on the left) and diamond adapted from Ibach and Luth [2] (shown on the right). C atoms in graphite adopt a three-fold sp^2 configuration with weak Van der Waals forces between layers. In diamond, the symmetry is tetrahedral, with each carbon in a sp^3 hybridised configuration forming four bonds to other C atoms.

Material	E	G	ν	K
Germanium	1.316	0.545	0.207	0.76
Silicon	1.629	0.666	0.223	0.979
Diamond	11.41	5.53	0.07	4.42

Table 1: Comparing isotropic elastic moduli of diamond with other covalent solids. Note the high Young's modulus and low Poisson's ratio, which can be interpreted as a measure of the planar extension in the x-y plane when subject to a compressive force in the z direction, for diamond. The units for the moduli are given in $\times 10^{11}$ Pa.

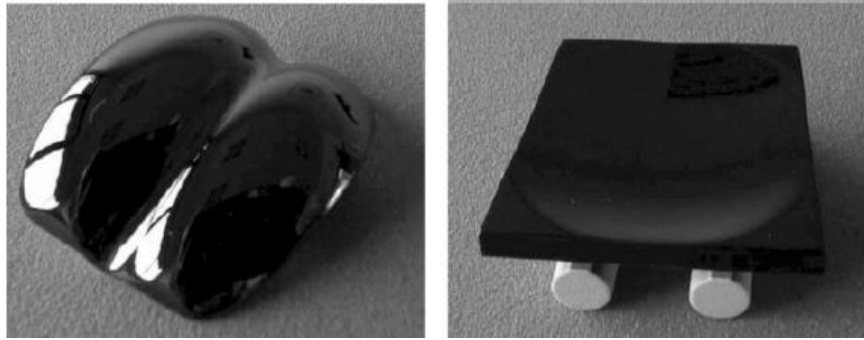


Figure 2: Diamond-coated ankle joint taken from [14]. The left shows the talar component and the right shows the tibial component.

1.1.2 Thermal properties

Complementary to some of the mechanical properties discussed above, diamond possesses a high thermal conductivity of $2300 \text{ W m}^{-1} \text{ K}^{-1}$ at $T=300\text{K}$ [20]. It should be noted that thermal conductivity is a function of temperature T and the trend from the same study is shown in Figure 3. This value is five times higher than for copper (Cu), a material already considered highly thermal conducting [21]. A completely isotopically pure sample of ^{12}C diamond may be able to obtain a thermal conductivity of $3500 \text{ W m}^{-1} \text{ K}^{-1}$ according to predictions [22]. The limitations of the thermal conductivity in naturally occurring diamond are due to phonon (collective excitations of atoms in the crystal lattice) scattering processes. Since naturally occurring diamond possesses an isotopic composition of 98.93% ^{12}C and 1.07% ^{13}C [20] scattering due to isotopes may contribute. However, defects may also contribute to the scattering. Naturally occurring diamond is known to contain nitrogen (N) impurities [23]. The literature distinguishes between diamond with low amounts of N (Type II) and those with higher amounts of N (Type I). Type I diamond can then be subdivided into Type 1a diamond, where the defects are substitutional and aggregate in a local area and Type 1b diamond, where N exists as individual substitutional impurities. Detailed discussion into defects is beyond the scope of this review, though the references given show how N defects may be characterised through spectroscopic techniques such as Fourier Transform Infrared (FTIR), electron paramagnetic resonance (EPR) and photoluminescence excitation (PLE) [24-27]. N is the most common impurity in naturally occurring diamond, but other impurities such as silicon (Si) may also be found [28]. Reducing the amount of N impurities in synthetic diamond is then clearly important in preventing the inhibition of desirable properties such as the thermal conductivity and optical transparency. However, the superbly high thermal conductivity of even a sample of type 1 diamond means that the material can function as a heat spreader, to dissipate heat from potential areas that may get hot during a device operation, for example in semiconductor devices. This is the case with gallium nitride (GaN) light-emitting diodes and high power transistor devices [29-30]. In both cases the purpose of a thin film diamond layer in the device is to spread heat uniformly before a heat sink in order to reduce device wear from

spots that are the consequence of a non-uniform distribution of heat. This same principle has also been utilised in laser diodes and vertical edge cavity surface emitting lasers [31-32].

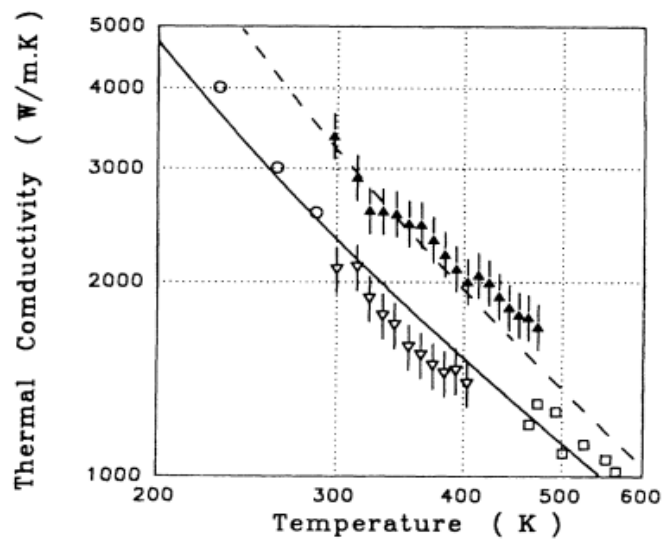
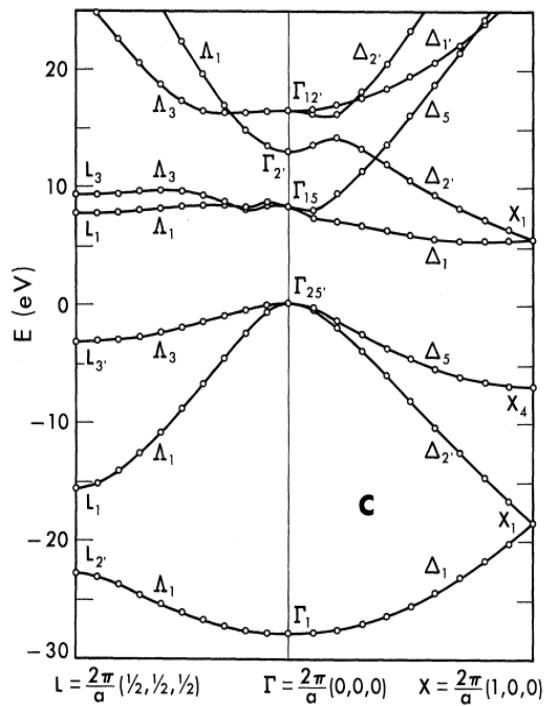


Figure 3: Trends adapted from [20] of thermal conductivity with temperature for single crystal diamond. The dashed line is a prediction for an isotopically pure ¹²C sample and the solid line is for natural abundance type 1a diamond.

1.1.3 Electrical properties

So far, the mechanical, optical and thermal properties of diamond have been discussed. In the case of the thermal properties, diamond was shown to be a suitable heat spreader material in the context of semiconductors. In terms of electronic properties, diamond naturally is an insulator material; with an even number of electrons per unit cell and no overlap between energy bands [2]. A calculated band structure is shown in Figure 4, which is the work of many different studies [33-36]. Table 2 complements Figure 4 with a comparison of theory with experiment. The point $\Gamma_{25'}$ denotes the valence band maximum E_v , while Δ_1 corresponds to the conduction band minimum E_c . Since the k-axis of the graph is in terms of the Brillouin zone wavevector k along points of high symmetry in the fcc crystal structure, it can immediately be observed that the band gap in diamond is 5.5 eV and indirect (E_v and E_c occur at different k), corresponding to a wavelength of 225 nm. Whilst diamond is an insulating material, it can exhibit semiconducting properties through n or p-doping. Addition of higher or lower valence elements than C result in gaining electrons or holes (which can be thought of as a lack of electron in a band, therefore carrying a wavevector $k_h = -k_e$). P-type doping of diamond is predominantly carried out with boron (B), while n-type diamond can be created through doping with sulfur (S), N or phosphorous (P). It should be noted that the dopants here are substitutional impurities on C lattice sites to contrast with doping that has also been carried out with lithium (Li) and sodium (Na) where the impurity

atoms occupy interstitial sites in the diamond lattice [37-40]. Figure 5 shows the energy levels produced by doping diamond with N, P and B.



	Theory (eV)	Experiment (eV)
Δ_{minimum}	(0.77, 0, 0)	(0.76 ± .02, 0, 0)
$\Gamma_{25'} - \Delta_1$	5.4	5.48
$\Gamma_{25'} - \Gamma_{15}$	7.3	7.3
$X_4 - X_1$	12.9	12.3-12.6
$L_{3'} - L_1$	10.9	9.5-10.5
$\Gamma_{25'} - \Gamma_{12}$	16.5	16-17

Figure 4: Band structure of diamond from [33].

Table 2: Comparison of band gaps from experimental and theoretical data.

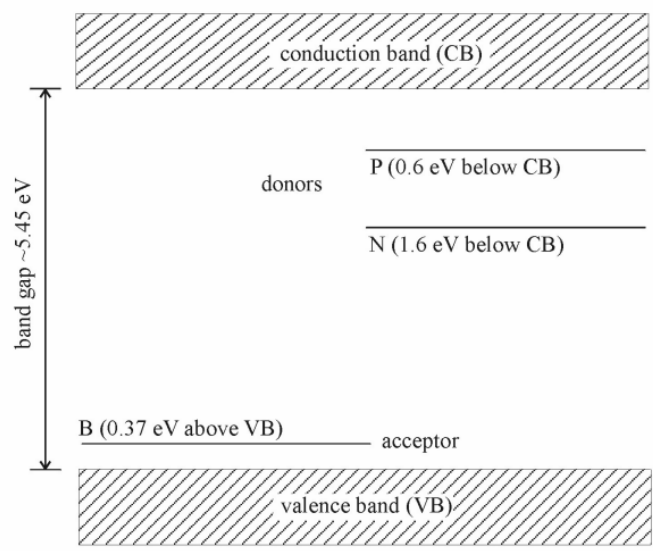


Figure 5: Energy diagram from [38] for diamond showing the levels produced by p-doping (B) and n-doping (N, P).

The realisation of diamonds semiconducting properties has been utilised in applications such as electrochemistry. Boron doped diamond has been used as an electrode for studies on the oxidation of phenol [41], hydrogen (H₂) and oxygen (O₂)

evolution [42] and reduction of nitrates to ammonia (NH_3) [43,44]. The use of diamond as an electrode is advantageous in the latter case since there is a wide potential window before H_2 evolution. Diamond electrodes also take advantage of their chemical inertness, which prevents the build-up of surface oxide layers common in other electrode systems and provides low adsorption properties along with the ability to operate in highly acidic media [45]. In a biological study of the electrochemical oxidation of histamine and serotonin it was found that boron doped diamond electrodes performed at signal to noise ratios an order of magnitude higher than polished glassy carbon electrodes in cyclic voltammetry studies [46].

Semiconducting diamond has not only been shown to be a great material for electrochemistry studies, but also as a material in high power electronic devices. The Johnson Figure of Merit (JFM) is a quantity that is calculated from the product of the electric field at breakdown E_B and the carrier saturation velocity v_{sat} . E_B is defined as the maximum electric field before dielectric breakdown where a normally insulating material becomes highly conducting and v_{sat} is defined as the maximum velocity a charge carrier gains before its kinetic energy (proportional to the square of the velocity v) reaches a constant value due to processes such as emission of optical phonons and defect scattering. Table 3 [47] lists E_B , v_{sat} and JFM values for various semiconductor materials. Before reaching v_{sat} , v is linear for low values of the applied electric field E . It is worth noting that for diamond the electron and hole mobilities (defined by the ratio of v to E in the low field limit) are very similar at around $2000 \text{ cm}^2/\text{Vs}$ [48], meaning their v_{sat} converge to similar values of $\sim 10^7 \text{ cm s}^{-1}$. This ultimately means that the high JFM for diamond is valid in the case of both n and p-doping. For high power electronics a high JFM is desirable in the case of high frequency operating field-effect transistors (FET). Figure 6 shows the demand for power and frequency for various applications [49]. In a high power operation it is clearly important that heat is dissipated throughout the device to stop hot spots from melting components leading to device degradation. From the previous section it was shown that diamond's high thermal conductivity allows it to function as a suitable heat spreader and ergo for FET applications, where low thermal conductivity and hence low heat dissipation may be a limiting case for other wide band gap semiconductors [50]. It should be noted that challenges exist in achieving FET performance with diamond, in particular exciting holes into the valence band from the acceptor energy level – for example from Figure 5 with B this is a gap of 0.37 eV. This energy is too great for thermal excitation at $T=300\text{K}$ ($k_B T = 4.1 \times 10^{-21} \text{ J} = 0.026 \text{ eV}$, where k_B is the Boltzmann constant with a value of $1.38 \times 10^{-23} \text{ J K}^{-1}$ and 1 eV is equal to $1.60 \times 10^{-19} \text{ J}$). Studies have found that the acceptor level decreases with increasing concentration of B [51, 52], meaning that full carrier activation can be achieved at room 300K. This has led to a concept called δ -doping, where a layer or multiple layers of p-doped diamond at a thickness of 1-2 nm are introduced into the structure. This is required so that the FET channel can be pinched-off by gate bias prior to reaching E_B [50]. The δ -doping has been used for diamond metal semiconductor field-effect transistors (MESFET), junction field effect transistors (JFET)

high electron mobility transistors (HEMT) [53-55] and research is expected to continue into the fabrication of high power devices. For an understanding of how field effect transistors work the reader should refer to Ibach and Luth [2].

There are challenges with n-doped diamond, which is the reason for only the p-doped diamond FET devices discussed in the previous paragraph. One reason stems directly from Figure 5, where the donor energy levels for P and N are 0.6 eV and 1.6 eV below the conduction band respectively. These energy levels are relatively deeper with respect to the gap between the acceptor and valence level for p-doped diamond. However, if the energies of the donor levels can be raised closer to the conduction band then the emergence of more n-type FET devices will be inevitable.

Johnson's figures of merit for a transistor's power and frequency performance for selected semiconductor materials

Material	E_B (V cm ⁻¹)	V_{SAT} (cm s ⁻¹)	$E_B V_{SAT} / \pi$ (V s ⁻¹)	$P_M F_L^2 Z_L = (E_B V_{SAT} / \pi)^2$ (W Ω s ⁻²)	Ratio to silicon (Dimensionless)
Silicon	3×10^5	1.0×10^7	9.5×10^{11}	9.0×10^{23}	1.0
GaAs	4×10^5	2.0×10^7	25.0×10^{11}	62.5×10^{23}	6.9
InP	6×10^5	2.0×10^7	38.0×10^{11}	144.4×10^{23}	16.0
GaN	20×10^5	2.5×10^7	159.2×10^{11}	2534×10^{23}	281.6
α -SiC(6H)	40×10^5	2.0×10^7	250.0×10^{11}	6250×10^{23}	695.4
β -SiC	40×10^5	2.5×10^7	320.0×10^{11}	10240×10^{23}	1137.8
Diamond	100×10^5	2.7×10^7	859.4×10^{11}	73856×10^{23}	8206.0

Table 3: From reference [47]. JFM values for various semiconducting materials. Note that diamond outperforms Si and gallium arsenide (GaAs) in terms of the JFM substantially. This is one of many motivations for research into diamond.

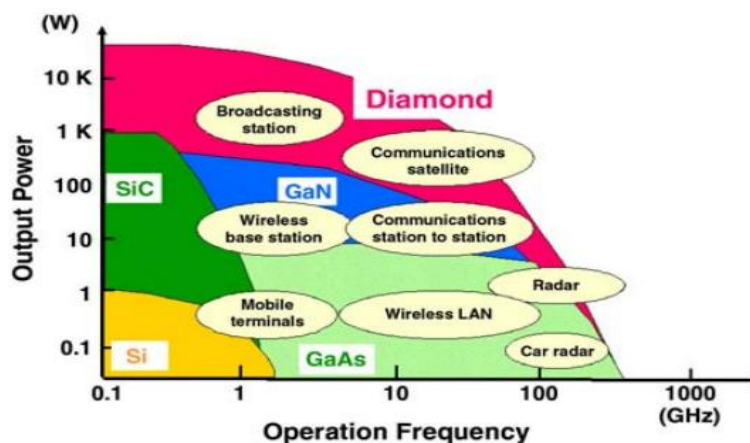


Figure 6: Graph of power and frequency demand for semiconductor devices, in particular FET's. It can be seen that diamond is most suitable for applications demanding high power and high frequency, whereas GaAs is only useful for high frequency, and silicon carbide (SiC) is useful for high power, low frequency applications.

1.2

Thin films and growth techniques

1.2.1

A note on amorphous carbon phases

Section 1.1 investigated the properties of natural diamond and thus a motivation for studying methods of thin film diamond growth for use in various applications. The literature refers to various carbon structures and derivatives. Diamond is a crystalline form of carbon entirely composed of tetrahedral coordinated sp^3 C atoms in a cubic lattice. Another form of crystalline carbon called lonsdaleite has a hexagonal unit cell and also consists of tetrahedral sp^3 C atoms and is sometimes referred to as hexagonal diamond though is much more uncommon than cubic diamond. In contrast to the crystalline carbons of diamond and lonsdaleite are amorphous 'diamond-like' carbon phases. In these phases the crystalline structure is disrupted by three-fold sp^2 C atoms [56]. Figure 7 shows a ternary phase diagram for amorphous carbon structures from [57]. At the extremes of sp^3 and sp^2 C structures without any hydrogen are diamond-like carbon (DLC) and graphitic structures respectively. Other phases exist in between such as tetrahedral amorphous carbon (ta-C) and tetrahedral amorphous hydrocarbon (ta-C:H) that exhibit the tetrahedral bonding of diamond but without the long-range crystalline order. Other amorphous carbons exist that do not exhibit the tetrahedral structure. The phases a-C and a-C:H are denoted amorphous carbon and amorphous hydrocarbon respectively. The a-C, a-C:H, ta-C and ta-C:H phases all have a mixing of the sp^3 and sp^2 C content with small (a-C, ta-C) or larger (a-C:H, ta-C:H) amounts of hydrogen. This affects the properties of the material substantially. Table 4 shows some hardness and band gap values obtained for various carbon phases [57-60]. It can be seen that the phases with less hydrogen (i.e. ta-C) tend closer to the diamond hardness value than higher H containing phases such as a-C:H. These amorphous phases may be produced by methods such as ion beam deposition [61, 62] where a DLC film is condensed from a highly energetic beam (~100 eV) of carbon or hydrocarbon ions generated from plasma sputtering of a graphite electrode in an ion source. The impact of the ions on the surface of a substrate induces sp^3 bonding, although sp^2 C may also be present. Other methods of growing amorphous carbon phases include cathodic arc sputtering [63, 64] and pulsed laser deposition from excimer (excited dimer) lasers such as ArF [65, 66]. The diamond-like film may be characterised in terms of the $sp^3:sp^2$ C ratio (i.e. to determine the phase by its position on the phase diagram in Figure 7) by techniques such as IR, Raman and electron energy loss spectroscopy (EELS) [67, 68]. In principle, the amorphous carbon phases represent a cheaper and faster alternative material to growing crystalline diamond but produces a diamond-like phase that does not exhibit the same strength, chemical inertness properties (particularly the phases with hydrogen included) of diamond. This review will now concentrate on synthetic diamond prepared from chemical vapour deposition (CVD).

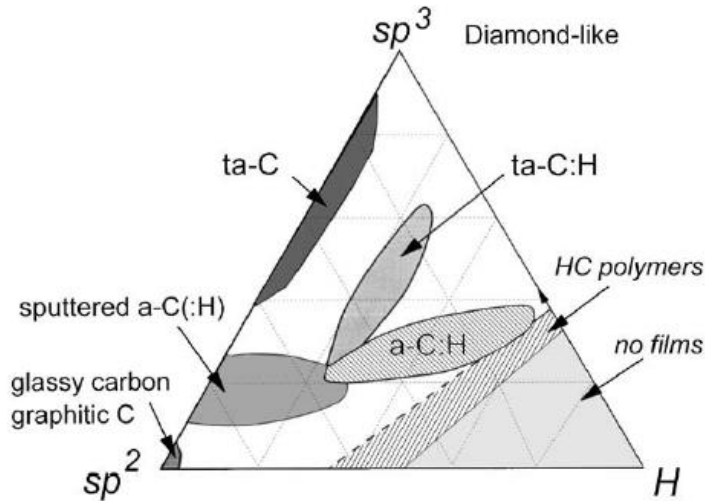


Figure 7: Ternary phase diagram for amorphous carbon structures.

	sp^3 (%)	H (%)	Density ($g\ cm^{-3}$)	Gap (eV)	Hardness (GPa)
Diamond	100	0	3.515	55	100
Graphite	0	0	2.267	0	
C_{60}	0	0		1.6	
Glassy C	0	0	1.3–1.55	0.01	3
Evaporated C	0	0	1.9	0.4–0.7	3
Sputtered C	5	0	2.2	0.5	
ta-C	80–88	0	3.1	2.5	80
a-C:H hard	40	30–40	1.6–2.2	1.1–1.7	10–20
a-C:H soft	60	40–50	1.2–1.6	1.7–4	<10
ta-C:H	70	30	2.4	2.0–2.5	50
Polyethylene	100	67	0.92	6	0.01

Table 4: From [57]. Comparison of diamond-like phases to diamond, graphite and buckminsterfullrene (C_{60}).

1.2.2 Crystalline phases: those prepared from chemical vapour deposition

Growing synthetic diamond and understanding the chemistry involved has been a challenge for a long time with a greater attention to synthesis in the 20th century. Initial efforts to grow diamond involved high pressures (50-100 kbar) and high temperatures between 1800-2300K [69-71]. Under these conditions, the diamond was produced by recrystallization of metal-solvated C where the metal was used as a catalyst to dissolve graphite and crystallize diamond. The phase diagram for elemental C, adapted from Bundy's original phase diagram [72] is given in Figure 8 [73]. The high pressure high temperature (HPHT) regime for diamond synthesis is marked in the figure for both catalysed and catalyst free regimes. Clearly, it is observed that the presence of a catalyst such as nickel (Ni) the growth of diamond can be achieved at much lower temperatures and lower pressure. The HPHT method is effective and accounted for a significant fraction of the diamonds grown for commercial applications between the 1950's and the 1990's. However, exploration into the low pressure regime where diamond is metastable was running

parallel to HPHT methods of producing synthetic diamond. One reason for this is because low pressure methods would be cheaper to run when producing synthetic diamond. Therefore, the focus for synthetic diamond then turned to gas phase deposition methods at lower pressures. Diamond is metastable at pressures ≤ 10 kbar pressure with respect to thermodynamics – graphite is the stable phase of carbon under these conditions for all temperatures. The enthalpy, $\Delta_f H$ and entropy, $\Delta_f S$ of diamond formation from graphite at 298K are $1.895 \text{ kJ mol}^{-1}$ and $-3.363 \text{ J mol}^{-1} \text{ K}^{-1}$ respectively [57]. Using the Gibbs free energy equation $\Delta_f G = \Delta_f H - T\Delta_f S$ this corresponds to a free energy of formation of 2.9 kJ mol^{-1} at 298K. From the negative value of the entropy it can be observed that with increasing temperature the diamond allotrope becomes less thermodynamically favourable with respect to graphite. Whilst diamond is not the thermodynamically favourable phase, the conversion of diamond to graphite is low, owing to a high activation barrier between the phases as the C-C bond energy in diamond is very high at 390 kJ mol^{-1} .

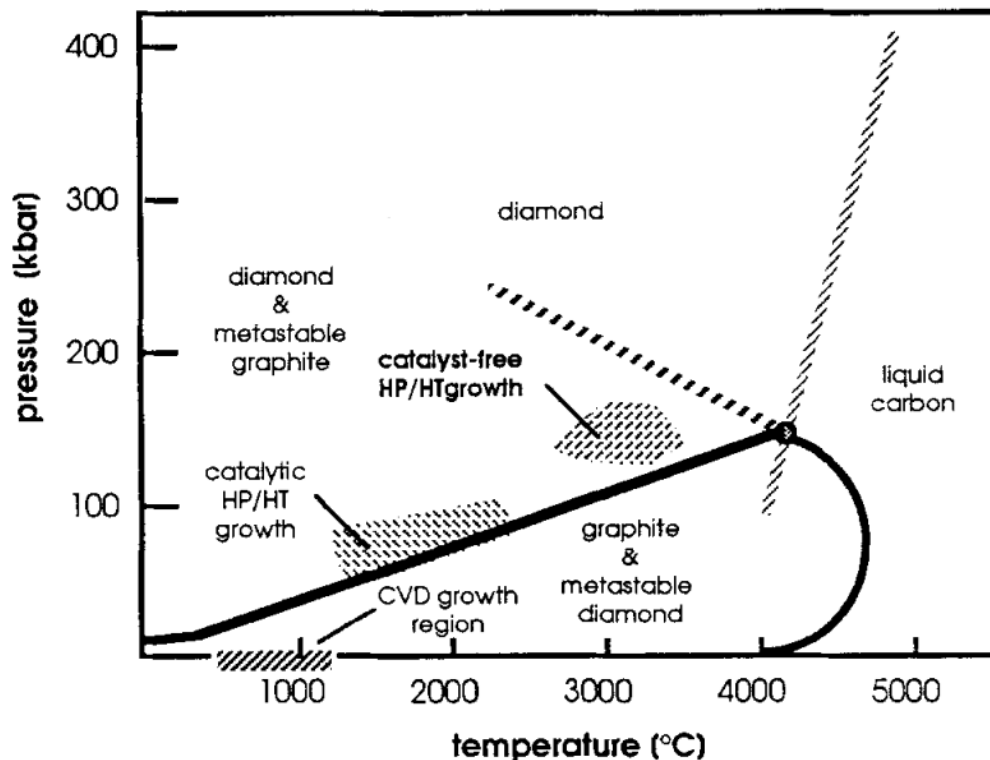


Figure 8: Phase diagram for elemental carbon adapted from Bundy [72]. The HPHT regimes are shown above the solid black line that separates the diamond and graphite phases. Below the line diamond is metastable with respect to graphite and vice versa above the line. The CVD region is of interest for the production of crystalline diamond films.

However, studies in the 1960's by Angus et al revealed that the purity of diamond crystals could be improved by the presence of atomic hydrogen to etch away graphite [74]. The study found that hydrogen etched both diamond dust and pyrolytically deposited graphite, albeit the rate of reaction for graphite was much

higher due to a lower activation energy barrier than that of diamond. They found that the optimal conditions for this process were $T=1033^{\circ}\text{C}$ and pressure $P=50$ atm where the loss of diamond was 0.22% and the loss of graphite was 99.9%. In the paper they state that lower pressures would further reduce the amount of diamond loss. Growth on non-diamond substrates such as Si, molybdenum (Mo) and tungsten (W) as well as diamond itself was shown in the 1970's [75, 76] though CVD was initially a slow method of choice for synthesizing diamond until the 1980's where growth rates of diamond were reported in orders of magnitudes of approximately $1\ \mu\text{m}\ \text{hr}^{-1}$ [77-80] via hot filament chemical vapour deposition (HFCVD) and microwave-plasma activated chemical vapour deposition (MPCVD). HFCVD and MPCVD form the most commonly used methods to grow diamond to this day. Other methods of growing crystalline diamond exist such as direct current (DC) plasma jet deposition, which was reported to grow diamond at nearly $1\ \text{mm}\ \text{hr}^{-1}$ in 1990. Diagrams for typical HFCVD, MPCVD and DC jet deposition are shown in Figure 9 from Bachmann [73]. A description of the three techniques are given below:

In HFCVD, a W, Mo or tantalum (Ta) filament is heated to temperatures around 2500K through electrical heating whilst the etchant gas (usually H_2) and hydrocarbons – mainly methane (CH_4) but also acetones, carbon monoxide (CO) and others can be used - are flown through the system at rates of 10^1 - $10^3\ \text{cm}^{-3}\ \text{min}^{-1}$ and dilute concentrations of carbon containing gas in a mixture of 99% H_2 1% CH_4 as a typical example. The temperature of the hot filament causes decomposition of the carbon containing gas and radicalization (decomposition) of H_2 . These reactions will be discussed in the context of MPCVD later. The substrate of which diamond growth occurs on is heated to roughly 1000-1200K by either the heated filament or an independent source to ensure diamond formation as opposed to amorphous carbon [81].

In MPCVD, similar gas mixtures are used to HFCVD. However instead using a hot filament to incite the gas phase chemistry (thermal activation), the chemical reactions are induced by a microwave plasma discharge, with the plasma maintained by constant microwave radiation. Typically the microwaves used are 2.45 GHz and are directed through by a waveguide. In the MPCVD reactor, the microwaves provide energy to electrons in the gas phase which in turn collide with molecules in the gas, causing heating, dissociation and excitation of gas phase molecules and in turn diamond growth on the substrate. The microwave power can be tuned between 0.1-5 kW to change the rate of growth, allowing up to $10\ \mu\text{m}\ \text{hr}^{-1}$.

In DC arc jet deposition, gas is flown at higher flow rates to that of MPCVD and HFCVD and is ionized by an electric discharge that forms a jet of ionized particles that approach the substrate at a high velocity. The pressure of the chamber for this technique is generally higher than that of MPCVD and HFCVD, going up to 1 atm pressure. The substrate has to be cooled in this technique as temperatures $> 1000\text{K}$ are not uncommonly observed and may cause damage to the substrate.

To compare and contrast the three methods, DC arc jet deposition offers the best growth rate, near 1 mm hr^{-1} but the deposition area is very small, being limited to the jet size which is typically 1 cm^2 . Non uniformities exist in the plasma jet temperature and consistent cooling of the substrate may cause thermal shock that will in turn damage the diamond film or potentially shatter substrate. HFCVD is a cheap method that can grow polycrystalline (this term will be discussed later) films of diamond at growth rates of $1\text{-}10 \text{ }\mu\text{m hr}^{-1}$ but suffers from filament material corroding the film as well as the filament itself being inherently sensitive to corrosion by the precursor gas mixture. This limits the options of gas mixtures available when using HFCVD. Using W as a filament also imposes a temperature limit of 2300K on the HFCVD method [82], slowing down the rate of diamond growth. However, this same study points towards Ta's performance that surpasses that of W in this region. MPCVD is the best method of the three described, eliminating the requirement of a filament and therefore all of the potential problems that may arise from filament corrosion as stated above with HFCVD. In addition to this, growth rates may be changed as a function of the microwave power and deposition can be carried out over a large area. The drawback of MPCVD is that it is much more expensive to operate than HFCVD or DC arc deposition methods.

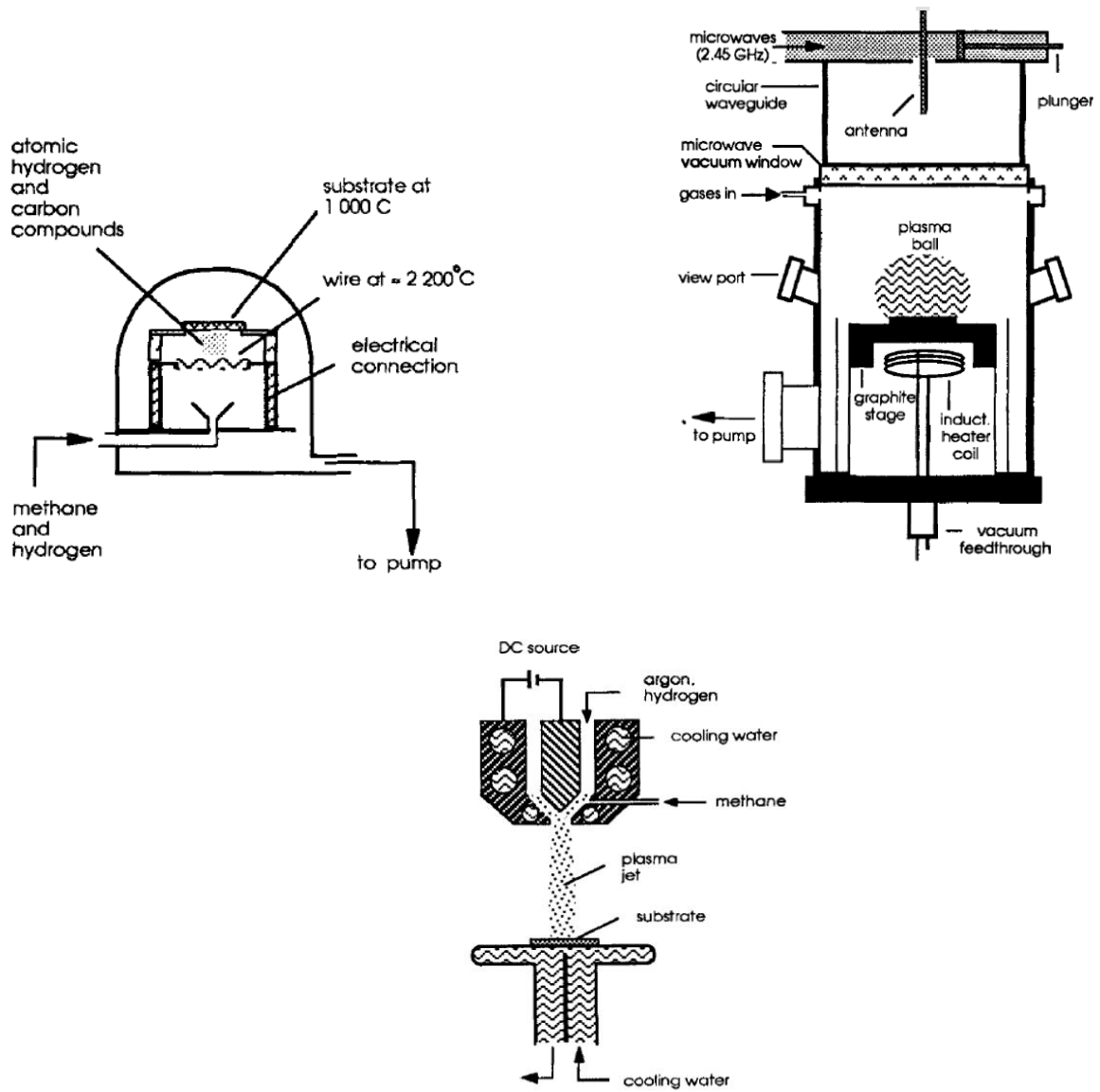


Figure 9: Typical HFCVD (Top left), MPCVD (Top right) and DC jet deposition (Bottom centre) apparatus. These three are the most common methods for growing diamond. From [73].

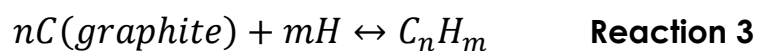
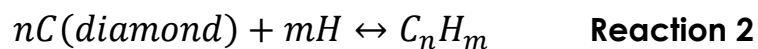
1.2.3

Growth mechanism of CVD diamond

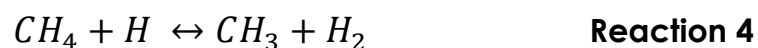
The growth mechanism of diamond on a substrate or diamond is to be explored in this section. It is noted that as discussed in section 1.2.2 that MPCVD allows for more different combinations of gas mixtures and thus the gas phase chemistry can get extremely complicated. However, there are some key reactions involved that will be discussed here. A diagram representing a simplified description of diamond growth is shown in Figure 10 from [83]. Source gases are flown in with their composition described as in section 1.2.2. Atomic hydrogen, H, is a very important candidate in the CVD process. H is formed from electron impact dissociation of H₂ in an MPCVD reactor or heat of the filament in HFCVD. Formally the reaction is:



Reaction 1 is generally thermodynamically unfavourable (reaction enthalpy $\Delta_r H = +456 \text{ kJ mol}^{-1}$, reaction Gibbs free energy $\Delta_r G = +155 \text{ kJ mol}^{-1}$) at $T=2500\text{K}$ [84]. However, recombination of atomic H to form H₂ is a three-body reaction and proceeds at a slow rate despite being energetically favourable. The atomic hydrogen functions in many ways. For example, it etches away graphite and diamond by the following reactions:



Where the rate of etching for graphite is much greater than that of diamond as described previously. Atomic hydrogen also takes a role in the activation stage through forming methyl (CH₃) radicals through the reaction:



Reaction 4 may be generalized for species CH_x as follows:

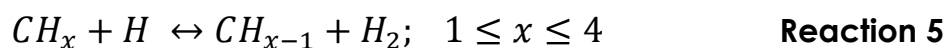


Figure 11 shows reaction 5 in successive steps. Also, the formation of C₂H_x species can be formed through reactions with CH₃ formed from Reaction 4 with other CH₃ and a bath gas M (Ar, He in figure 10) to form C₂H₆ or loss of H₂ to form C₂H₄. These steps are generally slow compared to the hydrogen transfer reactions given by reaction 5. Hydrocarbons containing more than two C atoms are generally not included as atomic H is able to break down long chain hydrocarbons into smaller products [81]. Transport of species to the substrate then occurs by diffusion, as experiments from Rau and Picht discovered [85]. The length scale of diffusion in an MPCVD reactor is on the order of several centimetres [86]. Hsu measured the mole fraction of hydrogen close to the substrate and found it to be on the order of

10^{-3} but much higher nearer to the plasma core, [87] indicating the diffusion-limited nature of the process. From a theoretical analysis, the MPCVD reactor operates in a low Peclet (Pe) number regime. The pecelet number is defined as follows:

$$Pe = \frac{\mu L}{D} \quad \text{Equation 1}$$

Where μ is the gas flow velocity, L is a characteristic length scale, in this case taken to be equal to the substrate diameter, and D is the diffusion coefficient for a particular gas. A low Peclet number regime, $Pe \ll 1$ signifies that transport of species is independent of the gas velocity. From defining a length scale for diffusion based on the spatial variation of the atomic hydrogen mole fraction as a function of the spatial coordinate z , which is a measure of the height above the substrate surface ($z=0$ therefore is on the substrate surface). This can be expressed as:

$$\left(\frac{dX_H}{dz}\right)_{z=0} = \frac{X_{H,Ref} - X_{H,0}}{l_d} \quad \text{Equation 2}$$

Where X_H is the mole fraction of H, l_d is a characteristic diffusion length for H, and $X_{H,Ref}$ and $X_{H,0}$ are the mole fractions of hydrogen at a reference point (for example in the centre of the plasma ball which lies on the order of mm-cm above the substrate and at the substrate surface respectively. Equation 2 effectively describes a concentration gradient for H. The ratio of $X_{H,0}$ to $X_{H,Ref}$ can be related through the expression:

$$\frac{X_{H,0}}{X_{H,Ref}} = \frac{1}{\left(1 + \frac{\gamma_H}{Kn}\right)} \quad \text{Equation 3}$$

With:

$$Kn = \frac{\lambda_H}{l_d} \quad \text{Equation 4}$$

$$\lambda_H = \frac{4D_H}{\bar{c}} \quad \text{Equation 5}$$

Where γ_H is the recombination coefficient of hydrogen atoms. This term is a coefficient of proportionality between the rate of recombination of H atoms and the concentration of H [86]. Kn is known as the Knudsen number and is a dimensionless quantity relating the length scale of diffusion and λ_H is a temperature, pressure and gas composition-dependent length scale. The temperature dependence comes from the thermal velocity c . λ_H is approximately equal to the mean free path. It can be observed from Equation 3 that in the limit that $Kn \gg \gamma_H$, that $X_{H,0}$ is equal to $X_{H,Ref}$. This limit means that there is effectively no concentration gradient of H. In the opposite limit that $Kn \ll \gamma_H$, equation 3 becomes:

$$\frac{X_{H,0}}{X_{H,Ref}} = \frac{Kn}{\gamma_H} \quad \text{Equation 6}$$

From equation 6 it can be observed that an increase in recombination or a decrease in the Kn (through an increase in λ_H which is intuitive as an increase in the mean free path corresponds to a lower mole fraction of H present) decreases the ratio of hydrogen mole fraction near the substrate surface relative to that in the plasma. Equation 6 defines the diffusion-limited regime of H transport. This is important when designing an MPCVD reactor as the diffusion limited nature of H transport has to be accounted for when designing the position (z) that a plasma ball sits above the deposition substrate. This will be covered in section 1.3.1.

Reaction 4 is of importance when discussing the mechanism by which diamond grows. The diamond lattice bulk is sp^3 hybridized, as discussed in section 1.1.1. However, at the surface of the diamond there is H termination, as shown in Figure 12. The H termination prevents the surface from constructing graphite and forming various cross linkages. During CVD growth atomic H created from reaction 1 can recombine (i.e. the backwards reaction) with a surface-terminated hydrogen to form H_2 . This reaction is more likely to happen at the substrate surface because the temperature of the substrate is around 1000K as opposed to 2500K in the centre of the plasma ball, or near the filament in a HFCVD reactor. This leaves a reactive carbon site in the diamond lattice. This will react with a CH_3 radical produced from reaction 4 for example to form a CH_3 bond where the H originally was. This occurs for all H terminated bonds on the surface, though only two are shown for clarity in the picture. Once C- CH_3 surface sites are formed, reaction 5 occurs with $x=3$ to form a CH_2 radical. The CH_2 radical then donates this electron to an adjacent CH_3 site to form a C-C bond. The C-H bonds on these two C atoms are then ready to repeat the process, building the diamond structure. It should be noted that this is a very simplistic mechanism for diamond growth, and that the actual process will involve many more reaction steps involving propagation reactions and other mechanisms describing how C atoms form on the surface. For an analysis of the rate constants and kinetics involved in many different reaction processes, see [88].

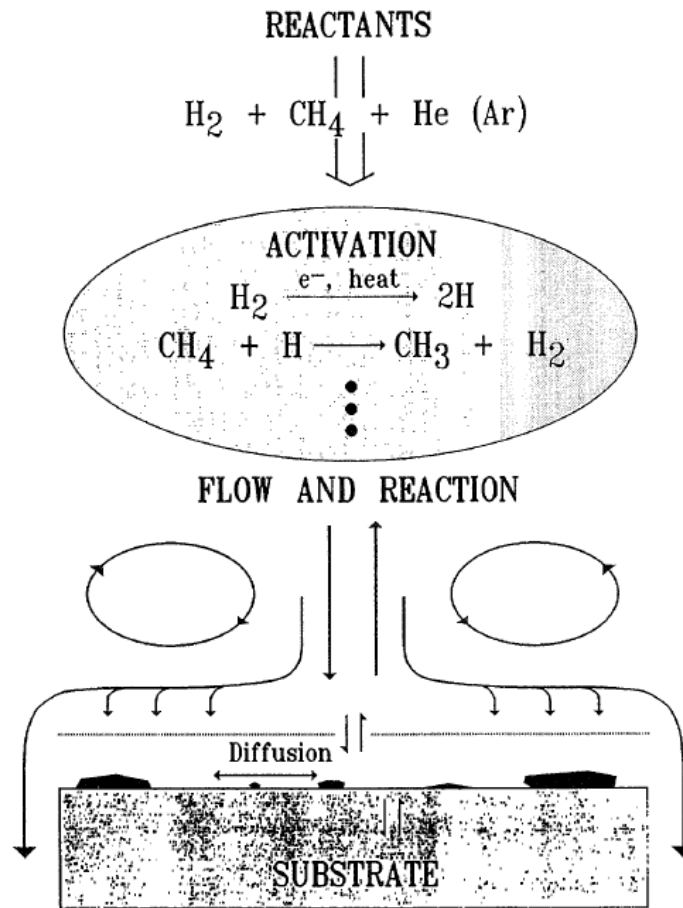


Figure 10: Simplified schematic of the CVD diamond growth process.

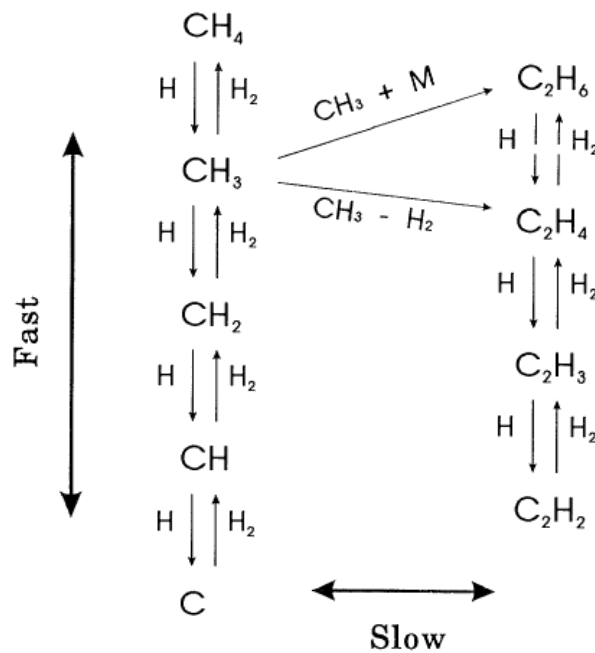


Figure 11: Diagram of H transfer reactions for species CH_x and C_2H_x as well as bimolecular reactions that convert between CH_x and C_2H_x species

1.2.4

Thin films and characterization

After a thin film of diamond has been grown, *ex-situ* analysis allows the thin film to be characterized. For thin films of diamond two techniques are widely used. Scanning Electron Microscopy (SEM) fires an electron beam into the sample and measures the intensity of backscattered primary and induced secondary electrons when interacting with the samples surface. This in turn produces an image of the sample that reveals topographical features including the crystallinity, defects in the form of dislocations, stacking faults and also an indication to any heavier (higher atomic number Z) elements present as SEM is a Z-contrast technique and so heavier elements appear brighter in the image. SEM also reveals the nature of the diamond grown – whether the film is single crystal or polycrystalline. The difference between a single crystalline and polycrystalline film is that the latter contains grain boundaries separating crystallites having potentially different orientations, whereas a single crystal consists, as the name implies, of one crystalline structure. The single crystal structure films of diamond are more desirable for applications such as electronics and optics but polycrystalline diamond is quicker to produce and will function effectively in mechanical applications such as coatings for drill bits. SEM images of polycrystalline and single crystal diamond are shown in Figures 13 and 14 [89, 90]. The single crystal diamond was grown on a diamond substrate in an MPCVD reactor employing the source gases H₂, CH₄ and O₂ with a CH₄/H₂ ratio of approximately 10%, microwave power of 2 kW and an overall chamber pressure of 150 Torr (760 Torr = 1 atm). The polycrystalline diamond was grown using also using MPCVD but with H₂ and CH₄ source gases in a CH₄/H₂ ratio of < 1%, with 1.2 kW microwave power and an overall chamber pressure of 45 Torr.

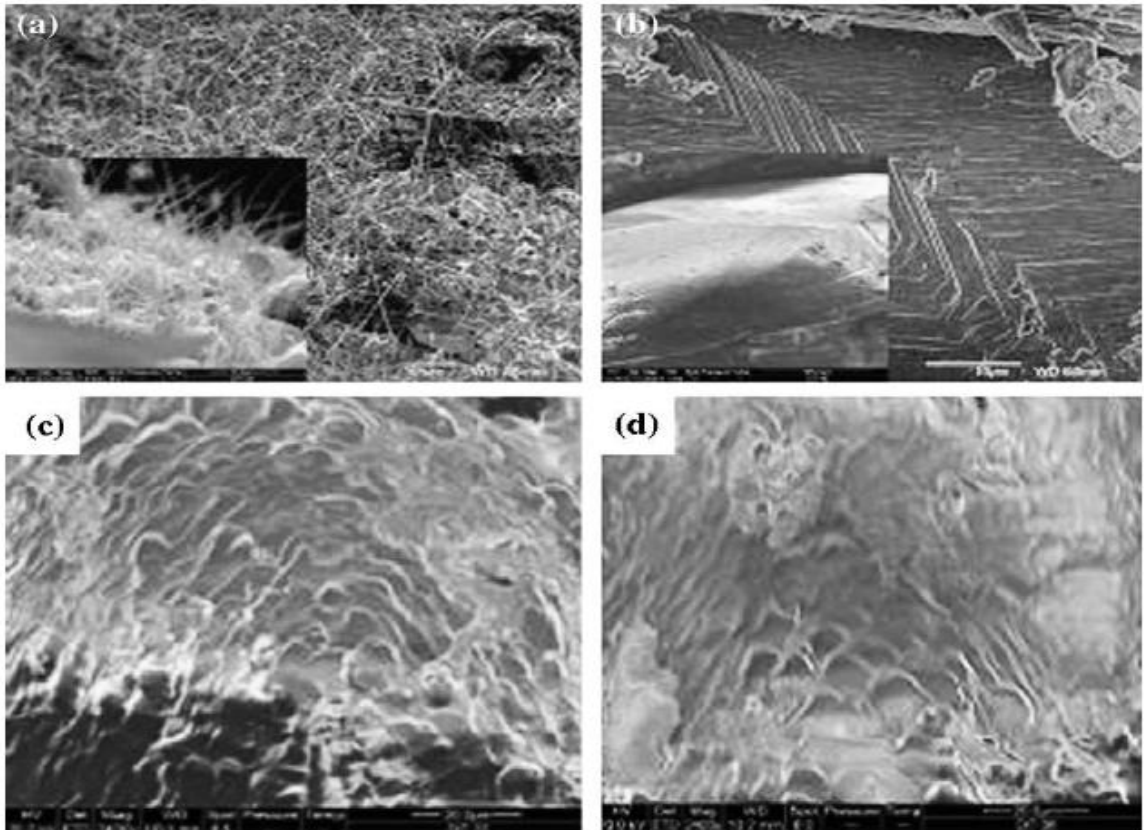


Figure 13: Scanning electron micrograph of single crystal diamond. (a) film grown with higher percentage of CH_4 source gas (b) image showing step growth of the single crystal structure (c) and (d) show the film morphology.

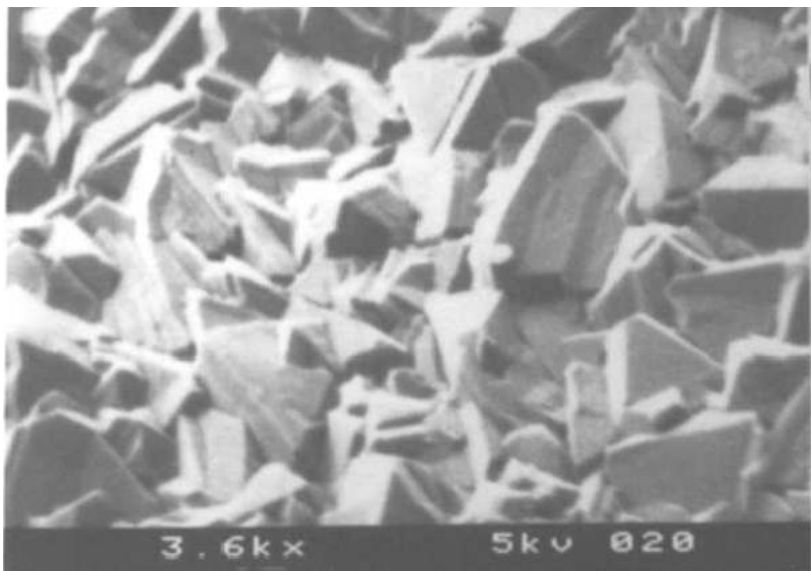


Figure 14: Scanning electron micrograph of polycrystalline diamond grown on Si

The second most common technique used to characterize thin films of diamond is Raman spectroscopy. The basic principle of Raman spectroscopy is a third order (nonlinear) interaction between the electric field of the incident electromagnetic radiation, usually in the form of laser light and the polarizability of the sample. The laser light provides energy to excite phonons in the sample. For more information on theoretical aspects of Raman spectroscopy see Douglas [91]. Diamond belongs to the space group $Fd\bar{3}m$ and its Raman spectrum consists of one Raman active peak belonging to a triply degenerate phonon with T_{2g} symmetry [92] that occurs at 1333 cm^{-1} . The peak is generally sharp. Figure 15 shows the Raman spectrum obtained for the single crystal diamond grown and characterized with SEM in figure 13. The result shows that the presence of oxygen (O_2) as a precursor gas decreases the width of the diamond peak. This width is described in terms of the full width at half maximum (FWHM) and is an indication of the purity of the thin film. It should be noted that the appearance of the Raman spectrum depends on the excitation wavelength [93]. Figure 16 shows Raman spectra of a polycrystalline film of diamond as a function of excitation wavelength. The progression from 1.16 eV to 4.82 eV represents a change in excitation wavelength from 1064 nm to 257 nm (from the IR into the ultraviolet region). It can immediately be observed that the FWHM of the diamond peak measured from this sample is much greater than that of the single crystal diamond. This may be the result of phonon confinement at grain boundaries. The study shows that using UV-Raman spectroscopy is better suited for characterization of diamond films than IR region Raman excitations, as fluorescence dominates the Raman signal at lower excitation energies. It should be noted that graphite also has a doubly degenerate phonon mode of E_{2g} symmetry that can be observed at 1582 cm^{-1} [94]. Since the scattering cross section of graphite is much larger than diamond, Raman spectroscopy can give a good indication of any surface graphitization that has occurred. In addition to this, UV excitation was found to enhance the peak intensity ratio of diamond to graphite by at least a factor of 25 [95]. This study also noted that overtones of the diamond peak (i.e. those of the energies $n \cdot 1333\text{ cm}^{-1}$, where n is an integer between 1 and 3) disappear with UV excitation. The overtones are of spectroscopic interest rather than for thin film characterization, as their features are weaker than the first order phonon. However, their absence in the spectrum is also desirable for characterisation purposes because it allows unambiguous determination of the hydrogen content from C-H bonds (with a detection limit of 0.001%) by taking the ratio of the 2930 cm^{-1} peak to the first order phonon line. UV-Raman spectroscopy has also been used to show the effect of decreasing crystallite size on the appearance of the first order phonon spectrum for nanocrystalline diamond films [96]. During the CVD growth process amorphous carbon may form under conditions where the substrate temperature is low. Figure 17 shows how the diamond-like phases of carbon affect the appearance of the Raman spectrum [57]. The spectra for amorphous carbons are therefore also dominated by the diamond and graphite phonons. The peak widths are wider than

those obtained for CVD or natural diamond and so the different phases are easily distinguishable through Raman analysis.

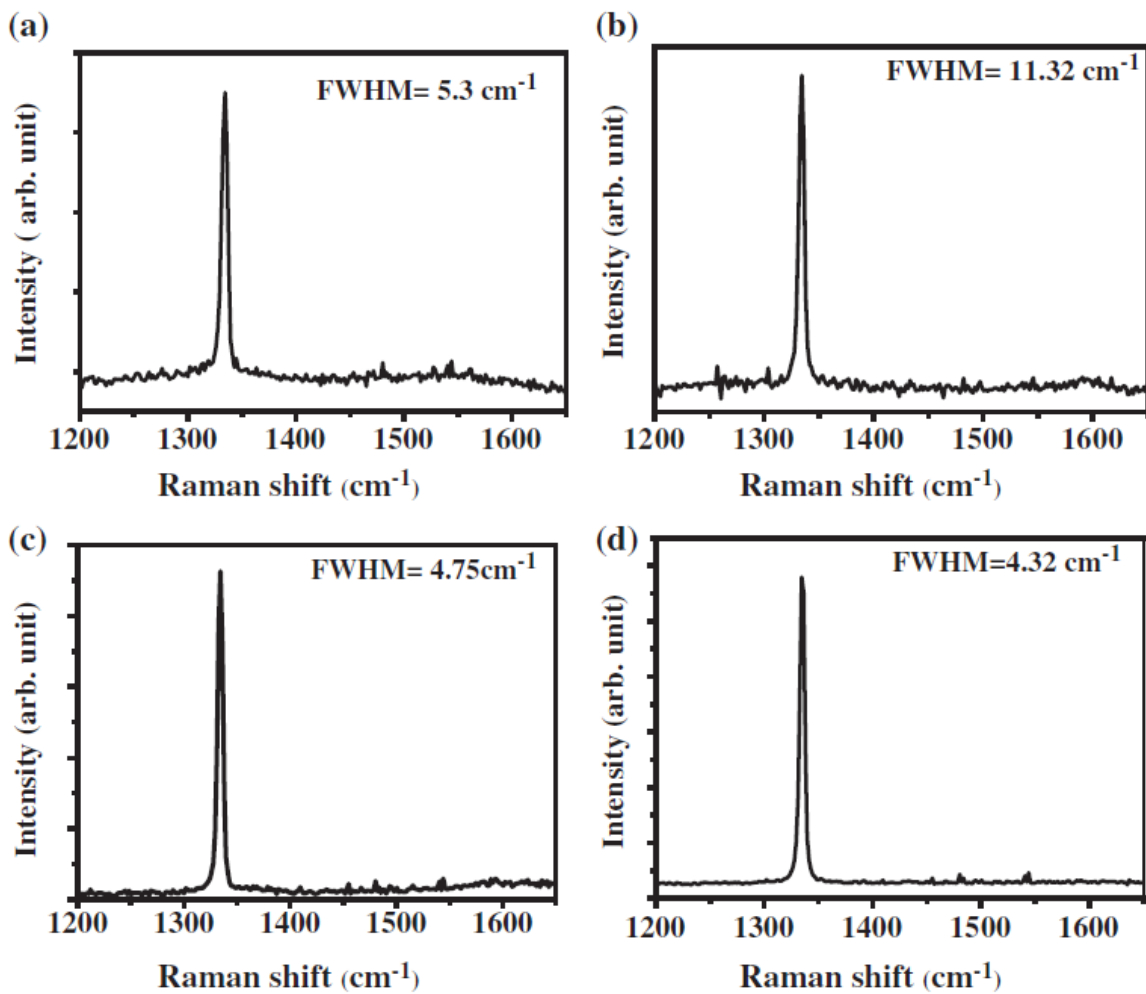


Figure 15: Raman spectra for MPCVD grown diamond with no oxygen (a) and flow rates of 0.25, 1.0 and 1.5 sccm

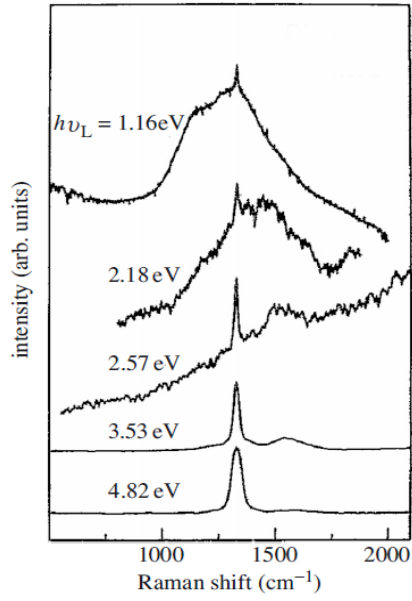


Figure 16: Raman spectrum of a polycrystalline diamond sample as a function of laser wavelength ν_L

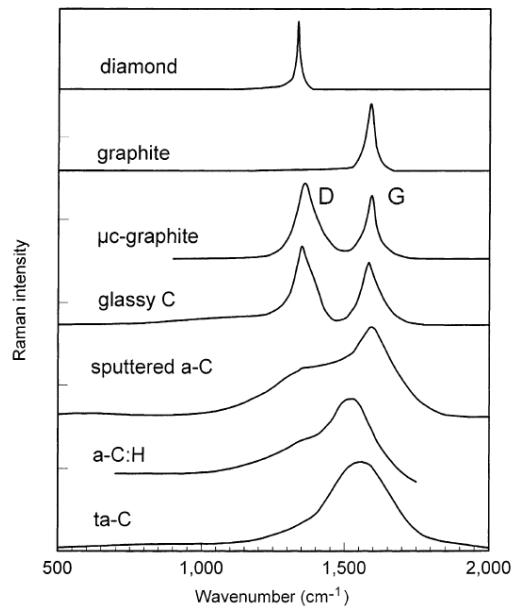


Figure 17: Appearance of diamond, graphite and amorphous carbon phases in the region of the first order phonon mode for diamond (1300-1500 cm^{-1}).

1.3

MPCVD

1.3.1

Principles of operation

Section 1.2.2 briefly described the principles behind how MPCVD works and a typical reactor design was also shown in Figure 9. This section will delve into more intricate details about MPCVD. The concept of MPCVD is based off of a microwave discharge which ignites the plasma. A microwave plasma discharge can occur and be maintained over a wide range of pressures, ranging from several atmospheres to weak vacuum (mTorr). In an MPCVD reactor the typical conditions entail flow rates of 1-500 sccm, where sccm is the standard cubic centimetre per minute ($\text{cm}^3 \text{min}^{-1}$) and an overall chamber pressure that is between 1-250 Torr. Microwaves are coupled in a water-cooled quartz cavity and directed into the reactor by a waveguide. The geometry of the waveguide determines what modes are allowed to propagate and in the case of an MPCVD reactor the geometry dictates which waveguide mode propagates. For MPCVD reactors like the one shown in figure 9 only one mode propagates through the reactor as designed by the chamber diameter and this is usually the transverse magnetic (TM_{01}) mode. In this mode the magnetic field is perpendicular whilst the electric field is parallel to the direction of wave propagation. Since the TM_{01} mode is not an allowed mode in a rectangular waveguide, an antenna is usually placed to convert the transverse electric (TE_{10}) mode that propagates through the rectangular waveguide to the TM_{01} mode that exists in the reactor cavity. The reason for using a TM mode as opposed to TE lies in electromagnetic boundary conditions – the metal cavity walls have a tangential electric field component of zero [97] meaning that the electric field has to be normal to the surface. This has the consequence that TE modes cannot have high electric fields near the walls, which means that ignited plasma will not be in contact with the sample holder thus not achieving maximum efficiency. The quartz window is necessary to limit excitation to an area near the sample holder, as regions of high electric field will exist in areas of the apparatus like the antenna and ignition of plasma there is undesirable. The electromagnetic fields in the cavity heat free electrons, enabling them to ionize gaseous species through collisions (this process is known as electron impact excitation), which leads to plasma ignition and sustainment. An important interaction to consider once the plasma is ignited is that between the plasma and the incident microwaves: the plasma absorbs and reflects microwave energy. This interaction can be described using an analytical model [98]. Using the z coordinate defined in section 1.2.3, the equation for a plane wave is:

$$E(z, t) = E_0 e^{i(\omega t - kz)} \quad \text{Equation 7}$$

Where E is the electric field, E_0 is the amplitude that may be a complex number to account for a phase difference not present in the exponential, ω is the angular frequency and k is the wavevector. The form of the wave represented in equation 7 assumes the wave travels in the z direction and that it is linearly polarized

in the x direction, which means that the magnetic field is in the y direction. The waves induce oscillations in the electrons in the x direction. The induced electron momentum is described by:

$$i\omega v_e + \nu_m v_e = \frac{eE}{m_e} \quad \text{Equation 8}$$

Where v_e is the velocity of the electrons, ν_m is the momentum transfer frequency that describes the change in momentum when electrons collide with gaseous species, e is the elementary charge on an electron given by 1.60×10^{-19} C, and m_e is the mass of an electron given by 9.11×10^{-31} kg. It is worth noting that due to the nature of the electric field, ionized species in the plasma are also subject to the electric field but are neglected due to their heavier mass relative to that of an electron. The plasma current density, j , may be written as:

$$j = -en_e v_e = \frac{\epsilon_0 \omega_p^2 (\nu_m - i\omega)}{\nu_m^2 + \omega^2} E \quad \text{Equation 9}$$

With:

$$\omega_p^2 = \frac{e^2 n_e}{\epsilon_0 m_e} \quad \text{Equation 10}$$

Where equation 10 is the plasma frequency, ϵ_0 is the electric permittivity of a vacuum, and n_e is the electron density. Maxwell's equations describe the propagation of EM waves in the plasma:

$$ikH = j + i\omega\epsilon_0 E = \left(\frac{\omega_p^2 (\nu_m - i\omega)}{\nu_m^2 + \omega^2} + i\omega \right) \epsilon_0 E \quad \text{Equation 11}$$

$$ikE = i\omega\mu_0 H \quad \text{Equation 12}$$

Where μ_0 is the magnetic permeability of vacuum and H is the magnetic field. From Equations 11 and 12 the wavenumber in the plasma is:

$$k^2 = k_0^2 \left(1 - \frac{p^2}{1+p^2} - \frac{iqp^2}{1+q^2} \right) \quad \text{Equation 13}$$

Equation 13 has both a real and imaginary component; these are given by the expressions:

$$Re(k) = \frac{k_0}{\sqrt{2}} \left[1 - \frac{p^2}{1+q^2} + \sqrt{\left(1 - \frac{p^2}{1+q^2} \right)^2 + \left(\frac{qp^2}{1+q^2} \right)^2} \right]^{\frac{1}{2}} \quad \text{Equation 14}$$

$$Im(k) = \frac{k_0}{\sqrt{2}} \left[\frac{p^2}{1+q^2} - 1 + \sqrt{\left(1 - \frac{p^2}{1+q^2}\right)^2 + \left(\frac{qp^2}{1+q^2}\right)^2} \right]^{\frac{1}{2}} \quad \text{Equation 15}$$

Where p is defined as the ratio of the plasma frequency to the wave frequency, q is the ratio of the electron momentum transfer frequency to the wave frequency. And k_0 is the wavenumber in vacuum defined by ω/c with c defined as the speed of light. There are physical implications to Equations 13-15. Equation 15 is the imaginary component of the wave vector for the incident microwave radiation. EM waves are absorbed by the plasma with a characteristic length scale is given by the skin depth, δ , which is the distance the microwave travels before its amplitude decays to e^{-1} of its original value. The skin depth in this case is given by:

$$\delta = -\frac{1}{Im(k)} \quad \text{Equation 16}$$

For efficient plasma creation, the skin depth has to be on the order of mm, which is a couple of orders of magnitude smaller a typical plasma size which is on the order of cm. This is because at smaller values of δ waves cannot effectively penetrate the plasma, and at bigger values of δ waves are not absorbed by the plasma. By considering the Poynting vector which is proportional to the cross product of E and H , the power absorption density P_{abs} at a location z may be computed as:

$$P_{abs} = \frac{|eE_z|^2 n_e}{2m_e \omega} \left(\frac{q}{1+q^2} \right) \quad \text{Equation 17}$$

The importance of equation 17 stems from its proportionality. The absorbed power is proportional to electron density in the plasma and is proportional to the ratio of the electron transfer frequency to the wave frequency. Analysing equation 17 shows that its maximum is when $q = 1$ i.e. $v_m = \omega$ and is zero when v_m is equal to zero. This expression suggests that in order to absorb microwave power in the plasma, electrons need to have collisions. Otherwise, the net gain in kinetic energy is zero because they are constantly experiencing acceleration and deceleration from the field. Energy is accumulated through electron collisions which the resultant velocities are in random directions; this means the electron acceleration becomes an irreversible process.

The plasma does not only absorb EM radiation but also reflects incident power. This can be derived through the boundary conditions for EM radiation. If E_i , E_T and E_R represent the incident, transmitted and reflected components of the electric field, and similarly for the magnetic field, the boundary conditions are:

$$E_i + E_R = E_T \quad \text{Equation 18}$$

$$H_I + H_R = H_T \quad \text{Equation 19}$$

Through analysing the form of the waves and substitution, an equation for the fraction of incident power reflected by the plasma surface R may be written:

$$R = \left| \frac{k_0 - k}{k_0 + k} \right|^2 \quad \text{Equation 20}$$

Typically, in most cases the reflected power is negligible and may be neglected. The analysis assumes an abrupt transition between the vacuum and the plasma.

Another key quantity in MPCVD reactors is the electron energy U . This is because it is related to the electron temperature T_e through the following relationship:

$$U = \frac{3}{2} k_b T_e \quad \text{Equation 21}$$

Where k_b is the Boltzmann constant as defined in section 1.1.3. The prefactor of three halves comes from the theorem of equipartition, which states that every degree of freedom contains energy of the magnitude $k_b T/2$. This therefore means that there are three degrees of freedom present for electrons which correspond to their translations in the x, y and z directions [99]. T_e is particularly important in plasma processes as it characterises a temperature at which electrons cause ionisation of gaseous species. This defines a plasma – a state of matter in which gaseous elements and ions exist. T_e generally depends on the composition of gases and therefore is observed to be constant within a given set of process conditions. The electron energy distribution function (EEDF) which describes the number of electrons with a given energy will therefore be a function of the T_e and n_e , however it may deviate away from a typical Maxwell-Boltzmann distribution significantly. T_e is generally a balance between the incident radiation absorbed due to the field, and energy lost in collisions. This is described as:

$$\frac{|eE_z|^2 n_e}{2m_e \omega} \left(\frac{q}{1+q^2} \right) = n_e N \kappa(T_e) \quad \text{Equation 22}$$

Where N is the gas particle density and κ is the energy loss coefficient which is a function of T_e . It can be observed that equation 22 is a balance between equation 17 and an energy loss term, meaning that the plasma is in a steady state. Since v_m is proportional to N , equation 22 can be rewritten as:

$$\kappa(T_e) k_m(T_e) \left[\left(\frac{w}{k_m(T_e)} \right)^2 + N^2 \right] = \frac{|eE_z|^2}{2m_e} \quad \text{Equation 23}$$

Where k_m is a coefficient of proportionality relating the electron momentum transfer frequency to the gas density. Equation 23 has two limits. In the limit of a small number of collisions in a given cycle i.e. $N \ll \omega/k_m$, equation 23 becomes:

$$\frac{\kappa(T_e)}{k_m(T_e)} = \frac{e^2}{2m_e} \left| \frac{E_z}{\omega} \right|^2 \quad \text{Equation 24}$$

In the opposite limit that there are many collisions per cycle i.e. $N \gg \omega/k_m$, then equation 23 becomes:

$$\kappa(T_e)k_m(T_e) = \frac{e^2}{2m_e} \left| \frac{E_z}{N} \right|^2 \quad \text{Equation 25}$$

Equations 24 and 25 reveal important aspects of plasma ignition. At low gas densities, T_e is determined by the ratio of the electric field to the wave frequency whereas at high gas densities T_e becomes determined by the ratio of the electric field to the gas density. This quantity is referred to in the literature as 'the reduced field strength'. This is important because the dependence of T_e on E/N suggests that sustaining the plasma requires less field strength than igniting it. This is because the gas density is much lower than at plasma ignition. From equation 10, and using the fact that the plasma frequency ω_p is at resonance from the microwave radiation with $\omega_p = 2\pi f$, where f is the frequency of the microwaves being generated (for example, 2.45 GHz), an upper limit on the electron density n_e may be calculated [100].

$$n_e = 1.2 \times 10^{-2} f^2 \quad \text{Equation 26}$$

Evaluating equation 26 for the case of an MPCVD reactor with microwaves being generated at a frequency of $f=2.45$ GHz amounts to an electron densities between 10^{10} - 10^{11} cm⁻³. In practice, the uses of waveguide applicators in microwave plasma etching experiments have suggested electron densities slightly higher than calculated through equation 26 [101,102].

1.3.2

Computational modelling of plasmas

Equations 7 through to 26 in section 1.3.1 described how the plasma absorbs and dissipates power as well as relationships of parameters that depend on the electron temperature and density. However, in order to understand the plasma dynamics, computational studies have to be carried out. This section will give a brief overview of computational studies modelling plasmas and the plasma chemistry in an MPCVD reactor. In order to describe the plasma-field interactions, Maxwell's equations must be solved using a finite difference time domain (FDTD) method [103]. The relevant Maxwell equations are:

$$\nabla \times E = -\mu_0 \frac{\delta H}{\delta t} \quad \text{Equation 27}$$

$$\nabla \times H = \varepsilon_0 \frac{\delta E}{\delta t} + j \quad \text{Equation 28}$$

Equations 27-28 describe the time-dependent nature of the electromagnetic fields in the cavity of an MPCVD reactor. In order to calculate the vector fields of E and H at every point in a defined region, the coordinates r and z must be defined. Equations 27 and 28 are expanded into six scalar equations in terms of the cylindrical coordinates [104]. A model cell for FDTD is shown in Figure 18. The electron transport equation and induced current density take similar expressions to equations 8 and 9 in section 1.3.1. In order to achieve a microwave excitation solution, the electron temperature and density parameters have to be calculated self-consistently using a fluid plasma model. The fluid plasma model is used to describe the behaviour of charged particles in a gas with a small degree of ionization. The equations solved in this model include the ion and electron fluxes, momentum and energy balance equations. When combined with Poisson's equation, which relates the second derivative of the potential with respect to distance to the charge density in a given region, the result is a self-consistent space charge field. These equations will not be shown, however they may be found in [104]. Figure 19 is a flowchart that represents the computational process for calculating parameters in a simulation using FDTD and the fluid plasma model. The input parameters typically involve the electron density, the power density absorbed by the plasma and the current density. The FDTD provides this output through solving the electron momentum transport equation. From this the plasma density and electron temperature are determined under steady state conditions. Iteratively, the power absorbed by the plasma will converge to a stable value where the electromagnetic fields and plasma characteristics are solved self consistently. Figures 20 and 21 show what may be achieved through computational simulations [97, 105]. The gas mixture used in simulations tends to be of H_2 only, because production of H ions (i.e. from reaction 1), recombination of hydrogen ions with electrons and ionization of H_2 (via electron impact) are the dominant processes responsible for creating charged particles in

the plasma. The rates for these processes are modelled with Arrhenius type expressions.

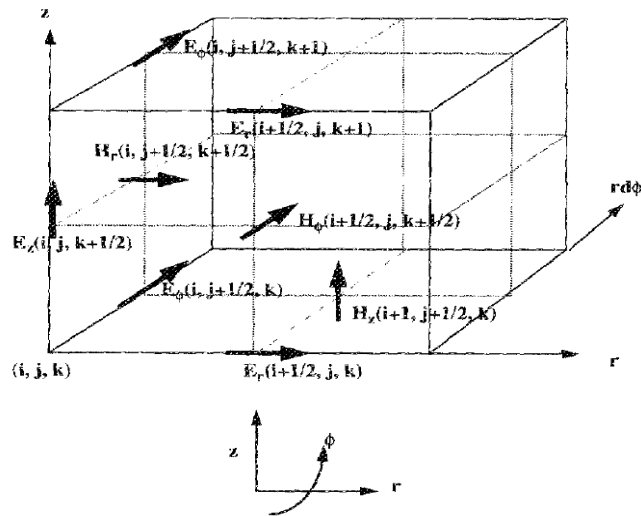


Figure 18: Typical FDTD cell for cylindrical geometry. A coordinate system is given below the cell. Within this cell, the electromagnetic fields of E and H are calculated at different steps.

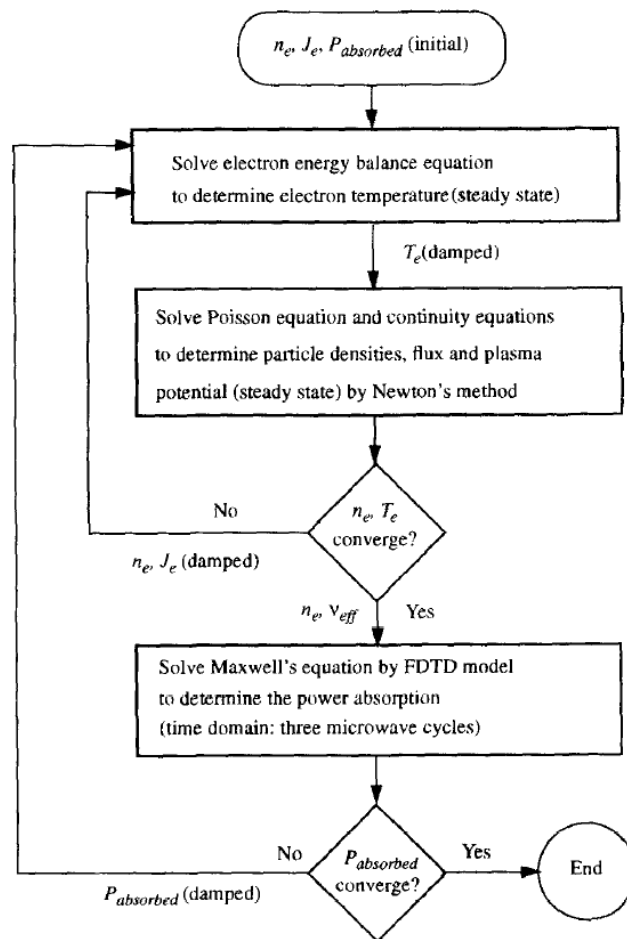


Figure 19: Flow chart for the numerical process of calculating MPCVD discharge characteristics in a self-consistent manner.

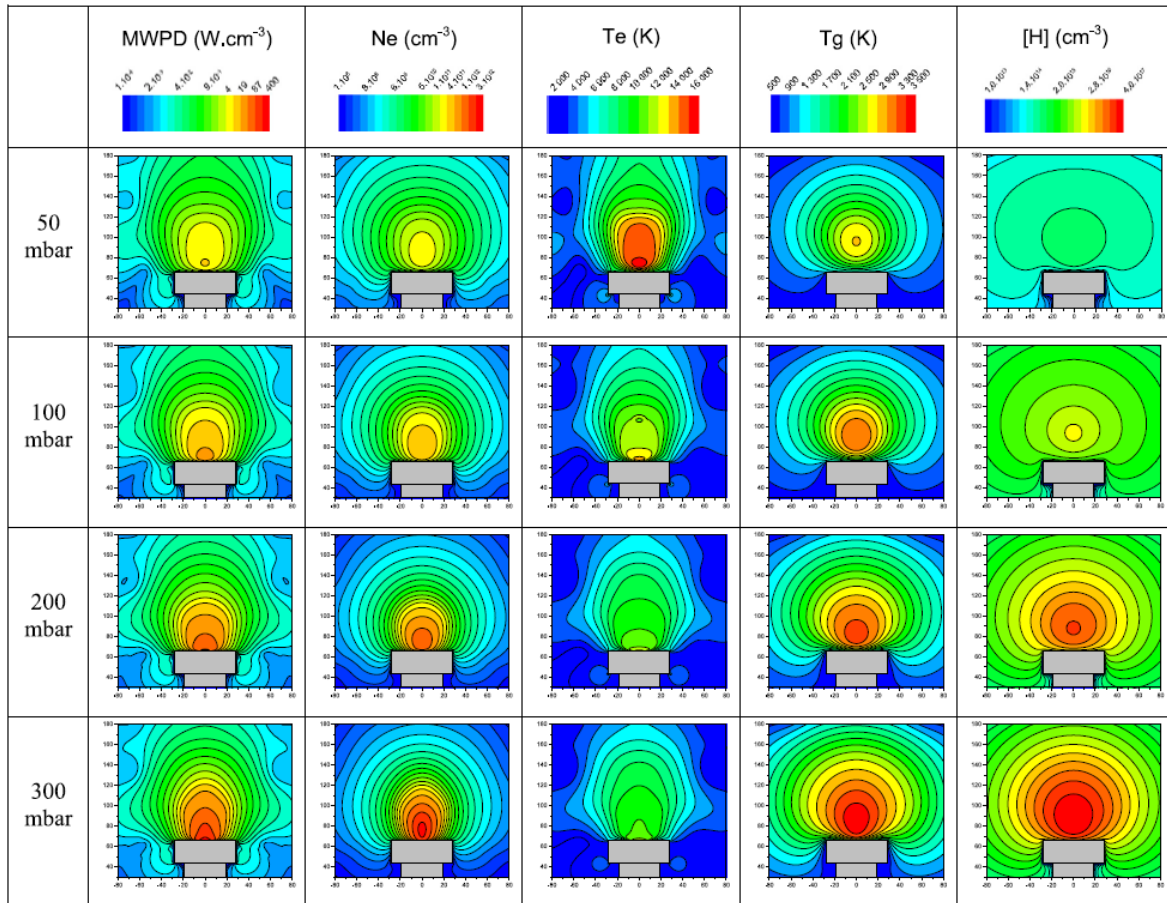


Figure 20: Variations of the microwave power density (MWPD), electron density N_e , electron temperature (T_e), gas temperature (T_g) and hydrogen concentration ([H]) as functions of overall chamber pressure between 50 mbar and 300 mbar. These parameters were calculated for a plasma that consists purely of H_2 using the principles given in this section.

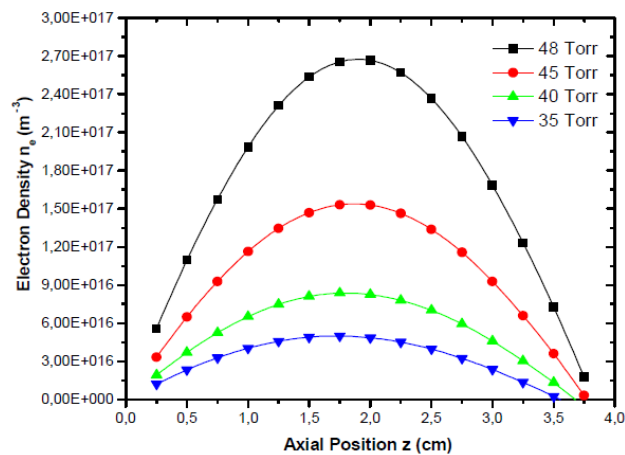


Figure 21: Electron density as a function of spatial coordinate z for a pure H_2 plasma. The curves represent different pressures between 35 to 48 Torr. It can be observed that the electron density is greatest at a position 20 cm above the substrate. The exact value of z for which N_e is greatest will depend on the substrate diameter, waveguide mode and reactor geometry.

1.3.3

Probing plasma characteristics

Section 1.3.2 demonstrated the ability to model plasma-field interactions through computational simulations. Experimentally, it is possible to gain information on the gas phase chemistry occurring within the plasma. This can be achieved through spectroscopic techniques. Both absorption and emission spectroscopies can give insight into the behaviour of species within an MPCVD reactor. Importantly, the reactor contains significant temperature gradients. For example, the gas temperature T_{gas} may be around 3000K in the plasma ball but significantly colder towards the reactor walls, decreasing to a value of potentially 300K. Because of the temperature gradients within the reactor it follows that the concentration of species such as [H], [CH₃] are functions of the radial coordinates r and z [106]. This was explored briefly in section 1.2.3, where the analysis showed the diffusion-limited nature of H transport. The presence of CH₃ radicals along with other hydrocarbons such as C₂H₂ and C₂H₄ have been monitored using line of sight absorption methods [107, 108]. Also, molecular beam mass spectrometry has been used to probe concentrations of radical and stable gaseous species under diamond growth conditions [109]. Absorption spectroscopy measurements can allow analysis of absolute densities of species within the plasma. However, the differences in temperature as a laser passes through the reactor and through the plasma ball are quite substantial. This means that the use line-of-sight absorption methods such as FTIR to provide absolute densities of a species of interest is quite hard as knowledge of transition moments for the spectroscopic transition must be considered through the range of gas temperatures. Emission spectroscopy is also used for plasma diagnostics. Optical emission spectroscopy (OES) is a technique used for studying plasmas that offers flexibility and high resolution. This technique relies on the light emission from higher lying states of species in the plasma that are formed from electron impact excitation of their ground state species. Figure 22 shows a comparison of OES data and cavity ring down spectroscopy (CRDS), a type of absorption spectroscopy that may be used to calculate absolute densities of species through their characteristic ring down time, which is the time taken for the original laser intensity to fall to e^{-1} of its original value. This analysis was carried out under typical MPCVD conditions of chamber pressure $p=150$ Torr, microwave power $P = 1.5$ kW, and flow rates of gases $F(CH_4) = 25$ sccm, $F(Ar) = 40$ sccm and $F(H_2) = 500$ sccm. The species being monitored are C₂ (a), CH (X, v=0) and H (n=2). The notation follows that X is the ground state, v is the vibrational quantum number, a is an excited state with a different spin to the ground state and n is the principle quantum number which determines the energy levels of the hydrogen atom i.e. $E=-13.6$ eV/n². The left hand y axis represents column densities on units of 10¹² cm⁻² and the secondary axis represent H atom densities in units of 10⁸ cm⁻². The OES data is scaled appropriately to compare trends with CRDS data.

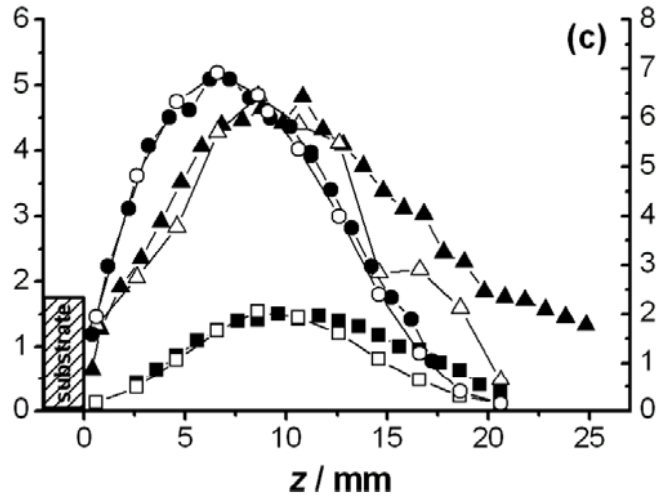


Figure 22: Comparison of OES data (open symbols) and CRDS data (solid symbols) for C2 (a, squares) CH ($X, v=0$, triangles) and H ($n=2$, circles). It can be observed that absorption and emission spectroscopy methods are complementary when probing plasma chemistry. From reference [106].

From figure 22 it can be observed that the densities of species in the plasma peak at heights > 5 mm. This is likely to be where the plasma core is given the H peak and arguments of the diffusive nature of H transport as discussed in section 1.2.3. The positions of peak maxima for other species will depend on the various reactions occurring in the MPCVD scheme. Thus, spectroscopy is a very powerful technique that enables plasma chemistry to be studied.

1.3.4

Motivation for study: N-containing plasmas

Sections 1.3.2 and 1.3.3 showed numerical and experimental methods for studying aspects of the plasma. MPCVD of diamond is a particularly complicated process and represents a challenge for scientists to understand the importance of various species that exist within the gas phase and how they lead to the production of CH₃ or indeed other C containing species that will build up the diamond structure following a reaction mechanism similar to that given in section 1.2.3. Also, challenges exist from a science and engineering perspective of achieving the highest growth rate possible of diamond through careful design of the reactor geometry, understanding the field distribution of the waveguide such that the plasma is ignited near the substrate (where the field induced energy transfer to the electrons is maximum) so that H₂ can be dissociated and play its role in propagating the formation of CH₃ radicals etc. An increase in growth rate does not necessarily have to be complimented by a high quality film of diamond, as discussed in section 1.2.4 in the case of polycrystalline and single crystal diamond, the application determines what is necessary. It was found that a small amount of N₂ present (100 ppm) increased the growth rate of diamond on all substrate orientations by at least a factor of two [110]. The findings from this study are shown in table 5. These results motivate the present project which aims to understand and compare aspects of the plasma chemistry for N containing plasmas with the precursor gases N₂ and NH₃.

Substrate orientation	Growth rate ($\mu\text{m/h}$) without nitrogen addition ^a	Growth rate ($\mu\text{m/h}$) with 100 ppm nitrogen addition
(111)	1.6	3.6
(110)	2.7	4.5
(100)	1.4	6.2
(100)+7°	1.5	8.0
α factor	1.5	3

Table 5: Comparison of the growth rate on a Mo substrate with and without N₂ in the precursor gas mixture. It can be observed that the growth rate is twice as fast on all substrate orientations. The α factor is related to the growth speed on the 100 and 111 directions and is not of interest here.

Experimental Details

2.1 *Brief description of the project*

The motivation for this project is based off of table 5 in section 1.3.4 that pointed towards a growth rate increase when N_2 was added to the precursor gas mixture. Understanding the gas phase plasma chemistry is therefore of interest for explaining these results. This project uses OES, which was described in section 1.3.3 to take spectra of emitted light from the plasma and perform analysis using a simulation tool called PGOPHER, which was developed at the University of Bristol by Dr. Colin Western to fit the experimentally obtained spectra to a model containing spectroscopic information about N_2 , NH and CN in order to determine information about the relative concentrations of species in the plasma and the gas temperature as functions of different parameters such as the microwave power, N_2/NH_3 flow rate and the spatial coordinate z . Results were carried out for both NH_3 and N_2 plasmas in order to compare and contrast differences in plasma properties.

2.2 *Apparatus and measurements*

2.2.1 *Apparatus*

The MPCVD reactor used in this study is the same as used in previous studies at the University of Bristol [111,112] and is shown in figures 23 and 24:

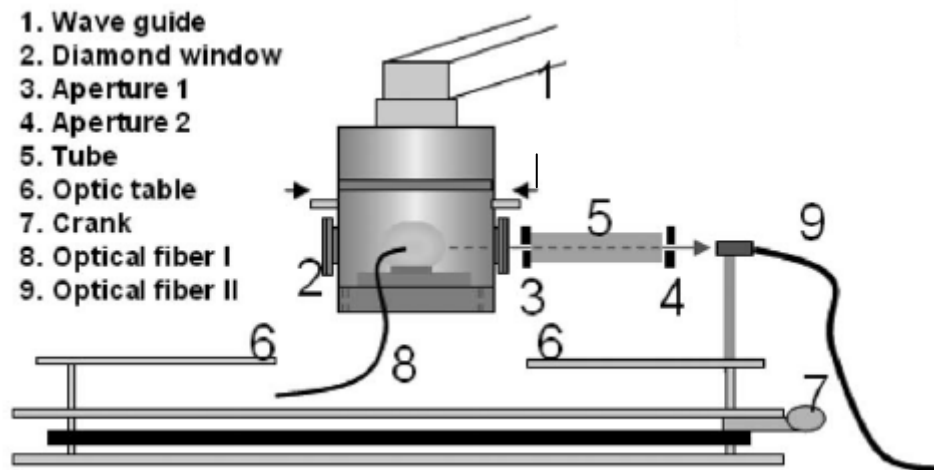


Figure 23: annotated diagram of the MPCVD apparatus. For this study, only optical fiber 1 was used.

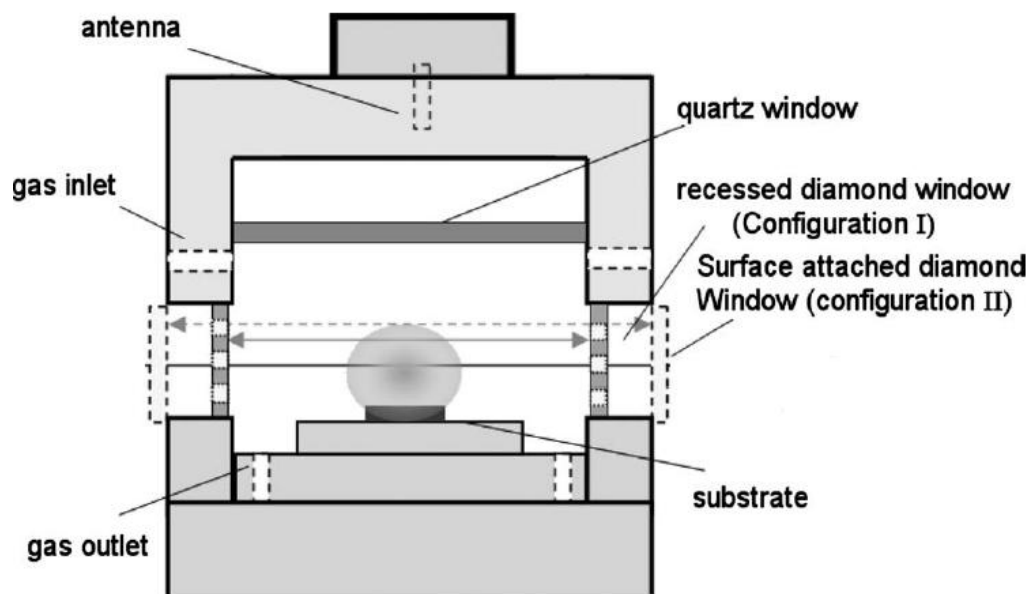


Figure 24: Another annotated diagram of the MPCVD apparatus, focusing on aspects inside the reaction chamber itself.

The principles of the reactor shown in figures 23 and 24 are very similar to that shown in figure 9 and the details given in section 1.3.1. Microwaves are generated at a frequency of 2.45 GHz and propagated in the TE₁₀ waveguide mode through the rectangular waveguide marked as 1 on figure 23. The range of microwave powers available for this apparatus varies between 0.6 kW and 1.85 kW. An antenna, as shown on figure 24, converts the TE₁₀ mode to the TM₀₁ mode which is then propagated through a quartz window into the chamber. The reactor has been designed such that the microwave discharge to form the plasma ball occurs at a height of roughly 3-8 mm above the Mo substrate marked in figure 24. Precursor gases of H₂, NH₃ and N₂ are flown into the reactor using mass flow controllers that allow easy alteration to the flow rate of gases. H₂ can be flown in up to 1000 sccm whilst NH₃ and N₂ can reach flow rates of up to 10 and 50 sccm respectively. The gas outlet leads to a vacuum pump that allows the chamber pressure to be regulated between 50 and 300 Torr in order to sustain the plasma. Light emitted from the plasma is transmitted through a diamond window. The emanating light is then passed through a series of optics in a tube marked 5 in figure 23 in order to collect and focus the diverging light through an optical fibre that leads to the OES spectrometer. In the spectrometer, the light passes through a series of optics and mirrors to correct for astigmatism and to finally disperse onto a detector, which collects the spectrum. The optic bench on which the optics described sit on has a crank denoted 7 in figure 23, which allows the height of the optics to be adjusted. This effectively alters the spatial coordinate *z* which allows measurements of spatial profiles, which will be discussed in section 2.2.2.

2.2.2

Measurements

The measurements carried out in this study were based on N₂/H₂ and NH₃/H₂ plasmas. Three different types of measurements were made. These are as follows:

Spatial profiles: variation of the spatial coordinate z . This was varied between $0 \leq z \leq 18$ mm, at $p = 150$ Torr, $P = 1.5$ kW, $F(N_2) = 3$ sccm and $F(NH_3) = 6$ sccm.

Microwave power: varying the power of the microwaves generated between $0.6 \leq P \leq 1.85$ kW, at $p = 150$ Torr, $F(N_2) = 3$ sccm and $F(NH_3) = 6$ sccm. Any variation in z will be denoted in the figure captions in the results. In general, they were all measured between 5-7mm.

Nitrogen flow: varying the flow rate of the precursor N containing gas. For N₂, this varied between $3 \leq F(N_2) \leq 35$ sccm and for NH₃ the range was between $1 \leq F(NH_3) \leq 10$ sccm. These results were carried out at $p = 150$ Torr, $P = 1.5$ kW, and the variation of z was subject to the same conditions as the microwave power measurements. These results will be expressed as mole fractions of the N containing gas flow through the relationship:

$$\chi_i = \frac{F(i)}{F(H_2) + F(i)} \quad \text{Equation 29}$$

Where i denotes the N containing gas i.e. N₂, NH₃. For the microwave power and spatial profiles, the flow rates of N₂ and NH₃ were chosen such to preserve the overall N atom flow rate. In this case the flow rates both correspond to an N atom flow of 6 sccm. OES spectra were taken with and without the Ncontaining precursor gas in order to isolate the N induced emission. An example OES spectrum from the measurements is shown below from flow rate measurements with N₂. The spectra obtained in this way were then simulated with PGOPHER, which will be discussed in section 2.3.

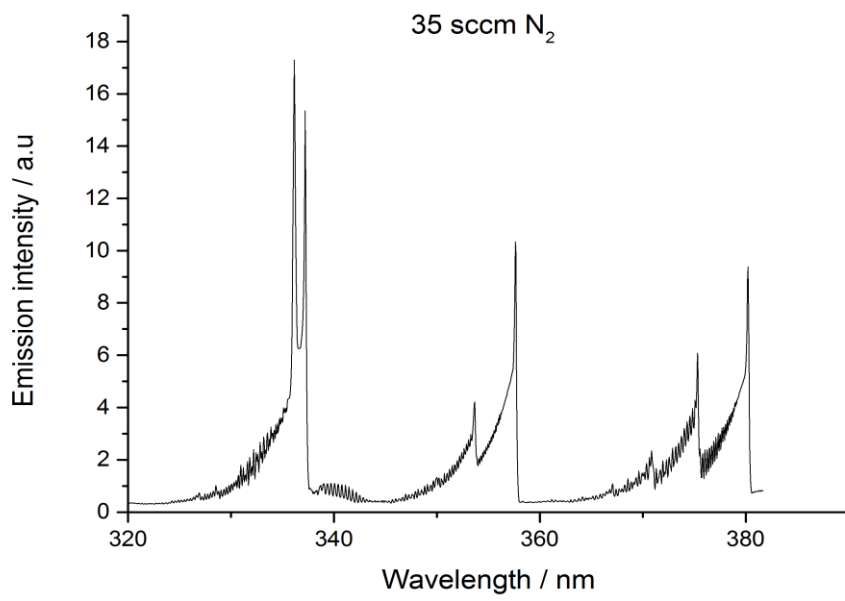


Figure 25: OES spectrum of flow rate measurements with $F(N_2) = 35$ sccm.

2.3

Using PGOPHER to fit experimental data

An experimental spectrum was shown in section 2.2.2. This experimental data was then fitted to a model in order to calculate quantities using a program called PGOPHER. PGOPHER is a unique piece of software to the University of Bristol that allows analysis of spectroscopic data. The program is able to simulate the spectra of molecules. In the case of the measurements taken, the transition that is observed is a near-UV(320-390 nm) electronic transition. Within this region, the following electronic transitions take place:



Where equation 30 represents the transition for N₂ and equation 31 represents the transition for NH. Equation 30 is well known in the literature as the second positive system of N₂, and shows vibrational fine structure as observed in Figure 25. The vibrational fine structure is due to the Franck-Condon principle, which states that an electronic transition takes place on a much smaller timescale than that of nuclear motions such as vibrations. This means that upon an electronic transition, the potential energy well for the excited state may have its minimum equilibrium separation distance r_e in a different location to the ground state potential energy curve. If an electron transition is to take place between these two states, it may find itself in a higher vibrational quantum number v when in the final state. Conversely, if the electron is in a higher vibrational state, it may be in a lower vibrational state in its new electronic state once the transition takes place. The strength of the different transitions is called the Franck-Condon factor. In addition to the Franck-Condon factors for various vibrational levels, the transition dipole moment is another important quantity which reflects the strength of the electronic transition. These parameters along with the vibrational band origins for $v=0,1,2,3$ and other spectroscopic correction constants were found for the transitions given in equations 30 and 31 and input into PGOPHER in order to simulate the spectrum shown on Figure 25 [113-115]. Figure 26 shows the experimental spectrum, the simulation spectrum and its individual components from PGOPHER. The peak overlap between NH and N₂ at a wavelength of 337 nm reveals an advantage of using PGOPHER to analyse the OES data compared to methods of determining quantities related to the concentration. Methods involving integration to calculate the area under the peaks will not work readily due to the peak overlap and therefore any measurement will give a concentration but unambiguous determination of the separate component concentrations is impossible without deconvolution of the peaks.

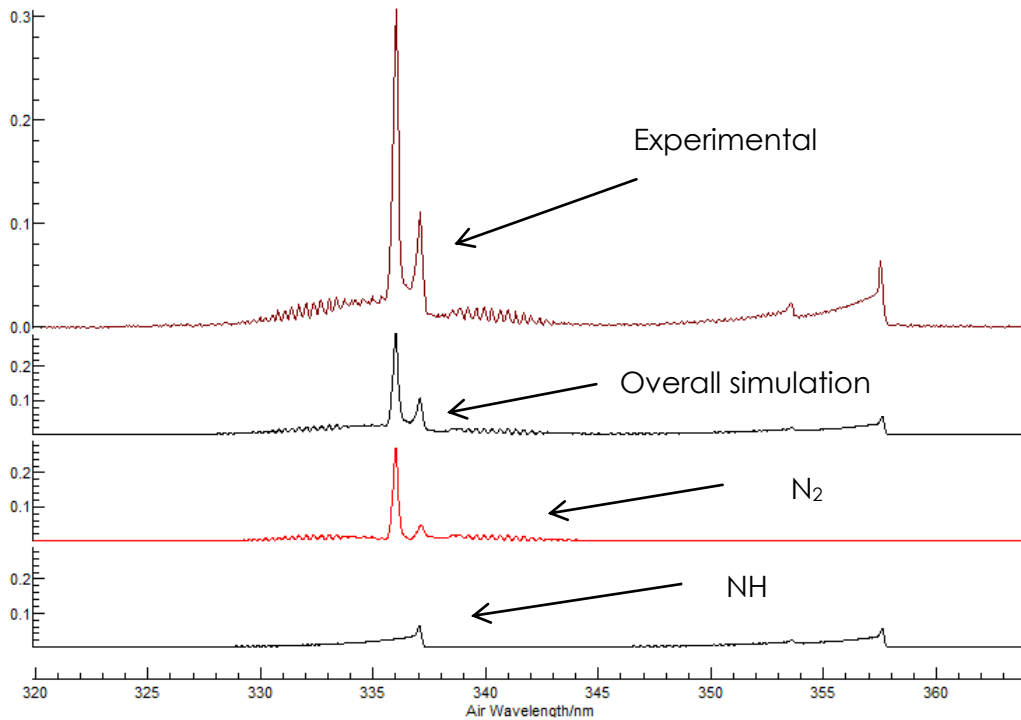


Figure 26: Graph from PGOPHER software. The graph shows simulation of the experimental data.

In order to fit the PGOPHER simulation to the experimental spectrum, the software calculates least-squares deviations of parameters allowed to change during the fitting process. These are called float parameters. The parameters floated for the fitting of the OES data consists of the gas temperature, T_{gas} , Gaussian linewidth, emission intensities of NH and N₂, and significant Franck-Condon factors. Figure 27 shows a log file that is updated with every fit. Figure 28 shows the experimental and resultant PGOPHER spectrum.

```
Contour fit to 319.667157479678 - 364.092217888694 nm (Points 475 - 1270) of 35N2.asc

796 Observations, 13 Parameters
Initial Average Error: 0.0167900046009045
Predicted New Error: 0.0167900045989872
Parameters:
```

#	Old	New	Std Dev	Change/Std	Sens	Summary	Name
1	2847.87920824838	2847.87949650917	33.86495	0.0000	1.74475	2848(34)	Simulation Temperature
2	.156878279310585	.156878230558215	.00866831	0.0000	.000385	0.1569(87)	Simulation Gaussian
3	9.32596859105045	9.32596936722118	.13417098	0.0000	.006482	9.33(13)	N2 Concentration
4	.993758473481366	.993758490050279	.00513316	0.0000	.000536	0.9938(51)	N2 <v=0 T(1) v=1> Strength
5	.774012735221541	.774012680959328	.01387136	0.0000	.001845	0.774(14)	N2 <v=1 T(1) v=2> Strength
6	2.7445095855271	2.74450976003631	.03138286	0.0000	.004129	2.745(31)	NH Concentration
7	-1.23534313098093	-1.23534327717804	.02391487	0.0000	.003624	-1.235(24)	NH <v=1 T(1) v=1> Strength
8	-1.34299905990053	-1.3429985099242	.01406386	0.0000	.000157	-1.343(14)	35N2.asc FrequencyOffset
9	1.00357673605022	1.0035767344634	4.2868e-5	0.0000	4.65e-7	1.003577(43)	35N2.asc FrequencyScale

Figure 27: Log file that is updated with every iteration of the fitting process. The table shows the old values of the floated parameters and their respective new values after a fit. Also shown is the standard deviation (Std Dev) and Change/Std, which is the change in the value from its old deviated by the standard deviation.

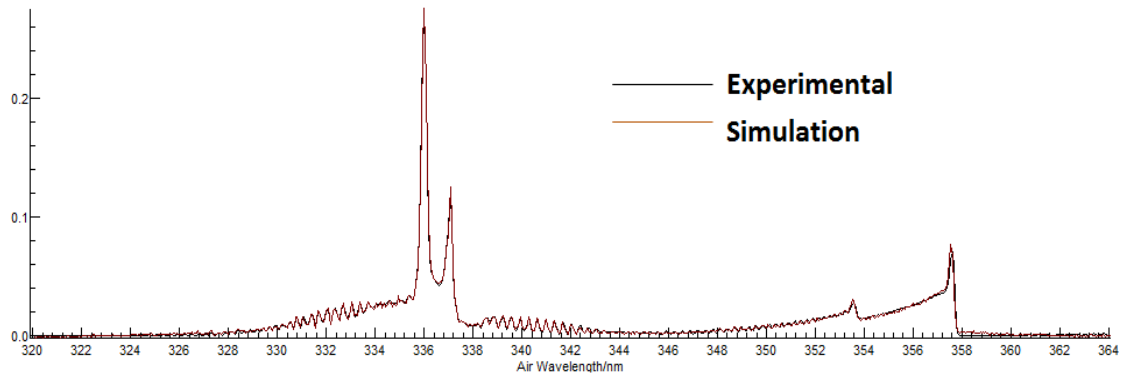


Figure 28: In-situ graph of the fitting process annotated with the simulation and experimental spectra. This demonstrates the high fidelity of PGOPHER for simulating electronic spectra.

The fitting process shown by Figures 27 and 28 was carried out for all OES data taken until the errors for all the float parameters were minimised (Change/std=0.0000 in Figure 27) and were then processed using Origin. The errors used were given by the standard deviation calculated from the PGOPHER fits and represents a single standard deviation (1σ) error. It is noted that this analysis could not produce absolute values of the concentrations. However, it is still possible to compare trends. The N_2 and NH emission intensities, T_{gas} and the ratio of $NH:N_2$ were analysed using this procedure.

Results

3.1

Spatial Profiles

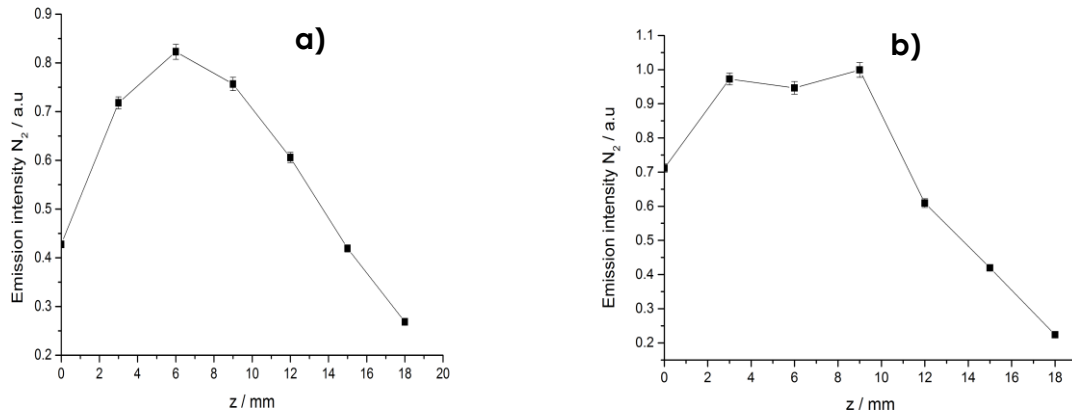


Figure 29: N_2 emission intensity as a function of z for a) N_2 and b) NH_3 containing plasmas. These experiments were carried out with $P= 1.5$ kW, $F(N_2) = 3$ sccm and $F(NH_3)= 6$ sccm.

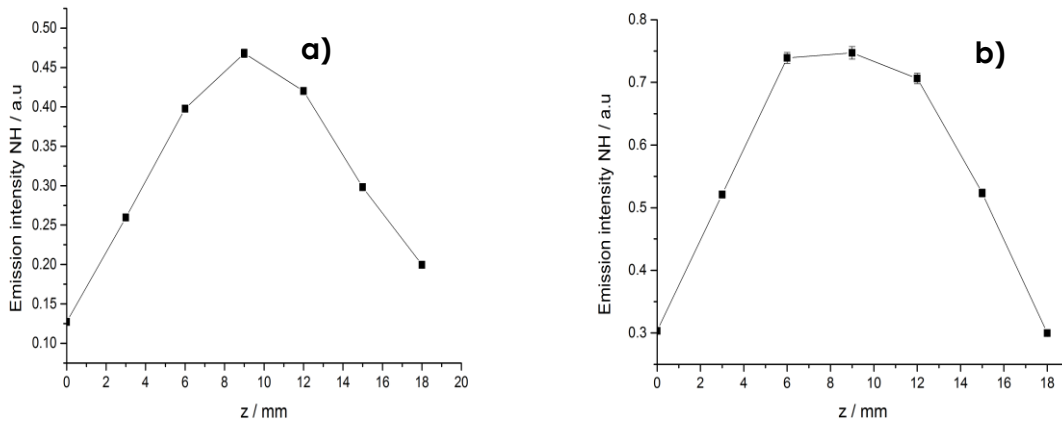


Figure 30: NH emission intensity as a function of z for a) N_2 and b) NH_3 containing plasmas. These experiments were carried out with $P= 1.5$ kW, $F(N_2) = 3$ sccm and $F(NH_3)= 6$ sccm.

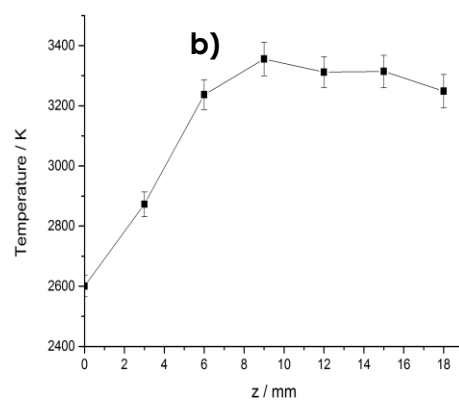
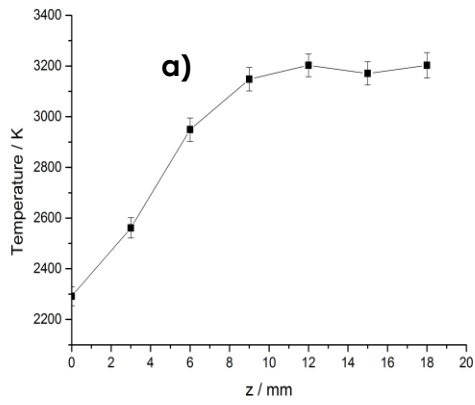


Figure 31: Gas temperature as a function of z for a) N_2 and b) NH_3 containing plasmas. These experiments were carried out with $P= 1.5$ kW, $F(N_2) = 3$ sccm and $F(NH_3)= 6$ sccm.

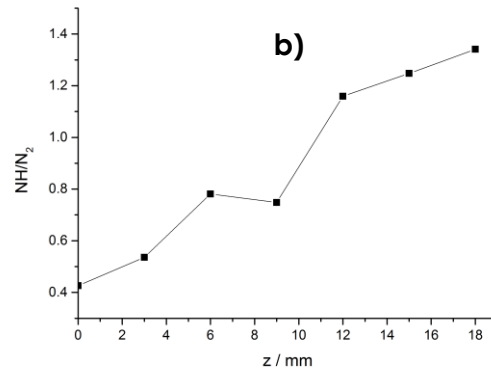
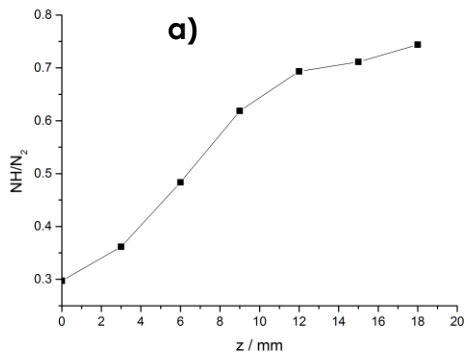


Figure 32: $NH:N_2$ ratio as a function of z for a) N_2 and b) NH_3 containing plasmas. These experiments were carried out with $P= 1.5$ kW, $F(N_2) = 3$ sccm and $F(NH_3)= 6$ sccm.

3.2

Microwave Power

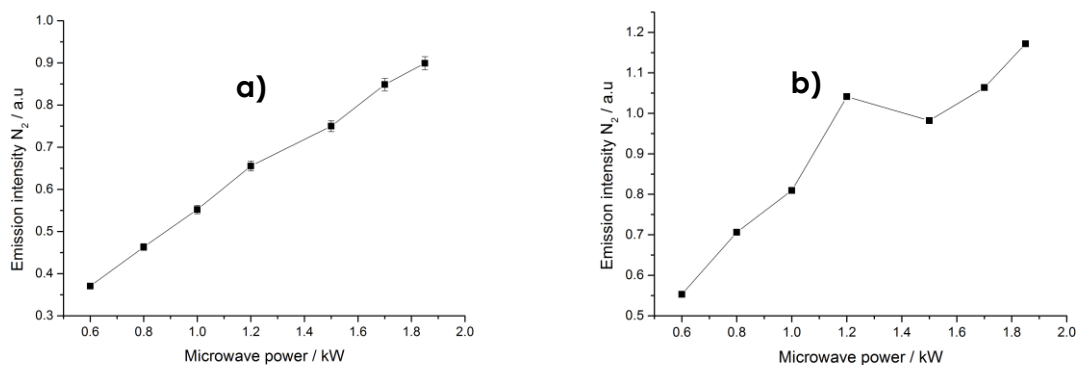


Figure 33: N_2 emission intensity as a function of microwave power in a) N_2 and b) NH_3 plasmas. These experiments were carried out with $z = 7$ mm for N_2 , $z = 5$ mm for NH_3 with $F(N_2) = 3$ sccm and $F(NH_3) = 6$ sccm respectively.

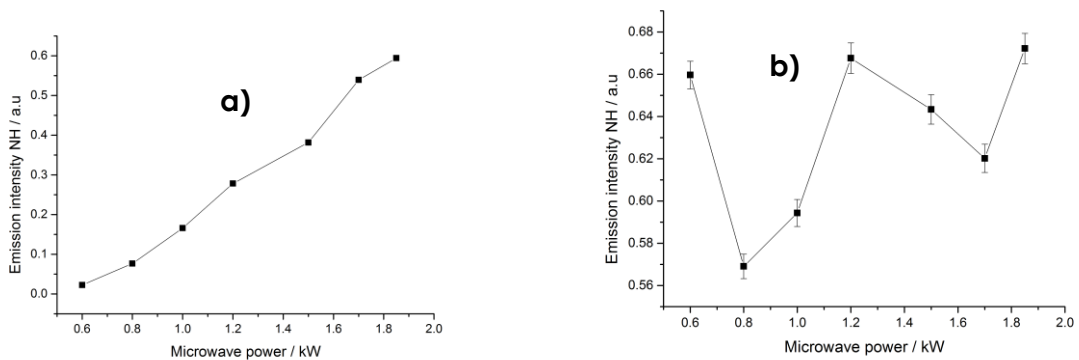


Figure 34: NH emission intensity as a function of microwave power in a) N_2 and b) NH_3 plasmas. These experiments were carried out with $z = 7$ mm for N_2 , $z = 5$ mm for NH_3 with $F(N_2) = 3$ sccm and $F(NH_3) = 6$ sccm respectively.

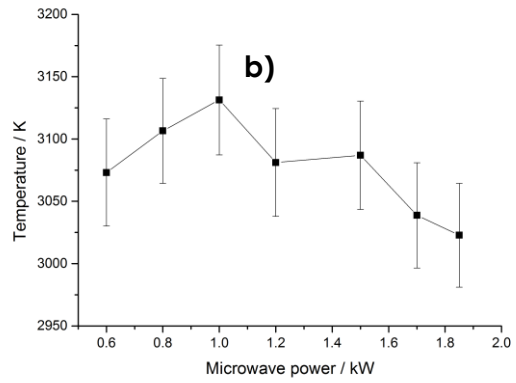
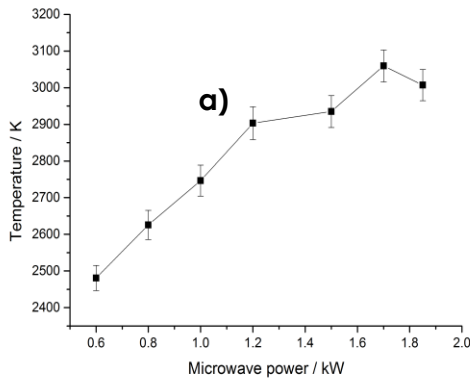


Figure 35: Gas temperature as a function of microwave power in a) N₂ and b) NH₃ plasmas. These experiments were carried out with $z = 7$ mm for N₂, $z = 5$ mm for NH₃ with $F(N_2) = 3$ sccm and $F(NH_3) = 6$ sccm respectively.

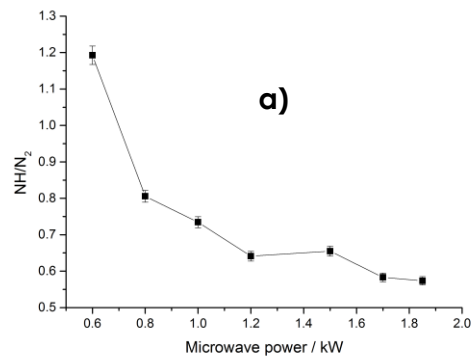
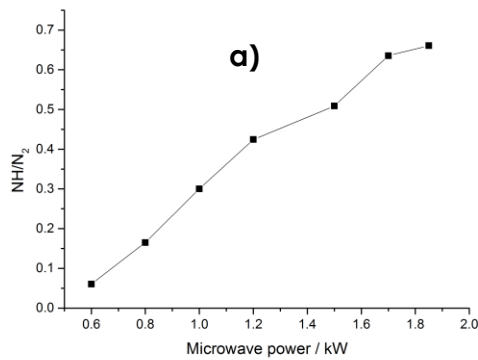


Figure 36: NH:N₂ ratio as a function of microwave power in a) N₂ and b) NH₃ plasmas. These experiments were carried out with $z = 7$ mm for N₂, $z = 5$ mm for NH₃ with $F(N_2) = 3$ sccm and $F(NH_3) = 6$ sccm respectively.

3.3

Nitrogen atom flow

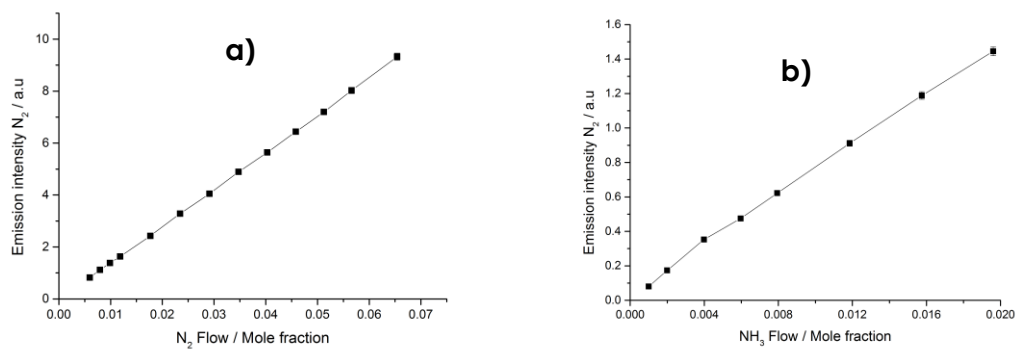


Figure 37: N_2 emission intensity as a function of a) N_2 and b) NH_3 flow in their respective plasmas. These experiments were carried out with $P= 1.5$ kW and $z= 7$ mm.

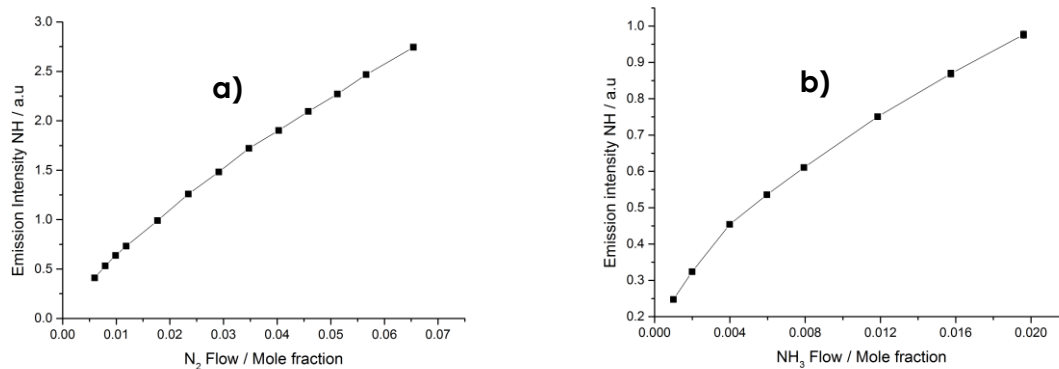


Figure 38: NH emission intensity as a function of a) N_2 and b) NH_3 flow in their respective plasmas. These experiments were carried out with $P= 1.5$ kW and $z= 7$ mm. The flows are expressed as mole fractions of the source gas.

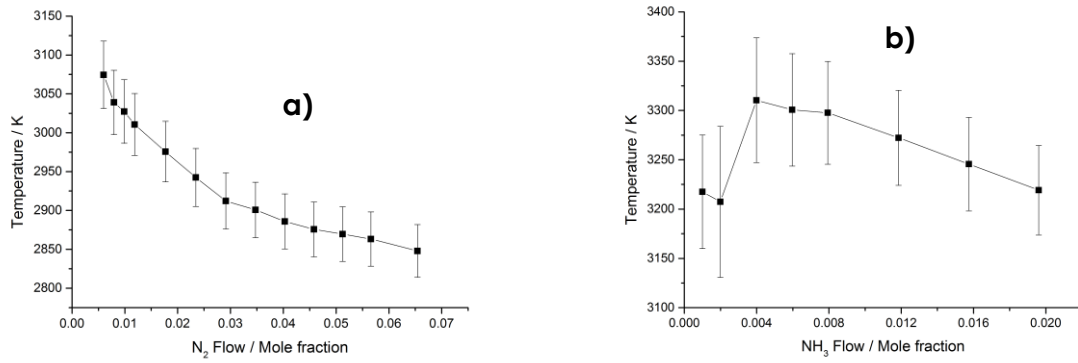


Figure 39: Gas temperature as a function of a) N₂ and b) NH₃ flow in their respective plasmas. These experiments were carried out with P= 1.5 kW and z= 7 mm. The flows are expressed as mole fractions of the source gas.

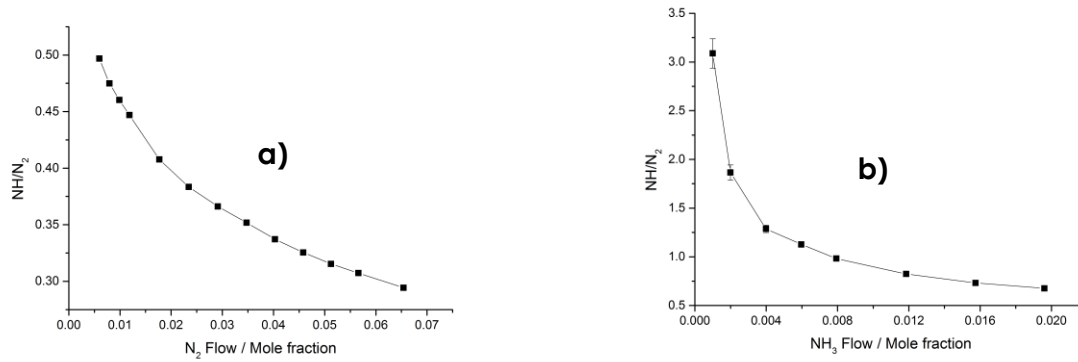


Figure 40: NH:N₂ ratio as a function of a) N₂ and b) NH₃ flow in their respective plasmas. These experiments were carried out with P= 1.5 kW and z= 7 mm. The flows are expressed as mole fractions of the source gas.

Discussion

The results in section 3 show similar and contrasting trends for both NH_3 and N_2 plasmas. The error bars shown for all graphs are 1σ either side of the data point and therefore their width is equal to 2σ . It can be observed in some results (for example, figure 40) that the error bars are small and therefore are not readily visible. The spatial profiles show that N_2 emission peaks at $z=7\text{mm}$ for both N_2 and NH_3 plasmas whereas the NH emission peaks around $z=10\text{mm}$ for N_2 plasma and between $7\text{-}10\text{mm}$ for an NH_3 plasma. $z=7\text{mm}$ is considered in the plasma core, however this could be easily be misinterpreted since the resolution offered by the spatial profile measurements is on the order of $\sim 2\text{mm}$. In order to remove ambiguity from determining the exact peak location of the NH emission the data should either be input into a model that describes the reactions of N_2 and NH_3 with H_2 with their respective rate constants and relevant plasma parameters following the FDTD method of modelling given in section 1.3.2. In addition to this, it is clear that a higher resolution measurement with OES may also assist in confidently assigning a peak height. However it may be observed that the N_2 emission is greater from a plasma containing NH_3 as a precursor gas. This can be observed by noting from figure 29 that the emission intensity for N_2 emission in the N_2 plasma is 0.8 whereas in NH_3 it is closer to 1. This is an unexpected result that cannot readily be explained by OES results alone; modelling of the plasma chemistry may compliment this result with an electron density map as a function of z . The difference in the N_2 emission from these plasmas may be explained by a greater electron density near $z=7\text{mm}$ in the NH_3 plasma. The gas temperatures follow similar trends as a function of z for both plasmas, as expected from discussions of H transport in section 1.2.3. The gas temperature is expected to drop on the order of 100's of K due to the diffusion-limited nature of H transport, which heats the gas. This is observed in figure 31 as z decreases from 7mm to 0mm , the gas temperature changes from $\sim 3200\text{K}$ to 2400K . However, the temperature remains constant above $z=7\text{mm}$ within error in both plasmas. This result cannot be explained readily; however one guess at an explanation might be due to the concentration of H being greater in this region. Therefore, the gas temperature is similar to the plasma core due to transfer of heat through collisions. Complimentary results of the mean free path and spatial profiles of H emission in this region may assist in confirming this case.

Measurements of the microwave power show linearly increasing trends for the N_2 emissions for both plasmas in figure 33. Again the N_2 emission from the NH_3 plasma is greater than that of the N_2 plasma. The reason for this is similar to the explanation given for the spatial profiles measurements. Since these results were taken at $z=5$ and 7 mm , they are near the peak maxima given in figure 29. The increase is due to microwave power providing more kinetic energy to electrons, which in turn produces a higher population of $\text{C}^3\Pi_u$ state N_2 molecules through the electron impact excitation process. This means that the transition given by equation 30 occurs more readily and therefore the emission intensity increases. A contrasting

result with the microwave power measurements is figure 35 which suggests the NH₃ plasma gas temperature is constant at approximately 3050K whereas the N₂ plasma gas temperature increases from 2500K up to 3100K. Both gas temperatures are constant within error at microwave powers ≥ 1.5 kW. A similar trend is observed in figure 34 for the NH emission intensity. These results are explained similarly to the N₂ emission. However, taking into account the dissociation energies of NH₃ and N₂ respectively explains the trend towards a constant gas temperature in figure 35. The bond dissociation energy for NH₃ is 4.5 eV, whereas for N₂ it is 9.8 eV [116, 117]. This means that the electron impact dissociation processes for the NH₃ (therefore explaining the constant value of the NH emission intensity) plasma are such that the energy imparted to electrons with 0.6 kW of microwave power readily dissociates NH₃. For N₂ a small fraction of N₂ will be dissociated into atomic N and available to react with atomic H (from Reaction 1 or otherwise) to form NH. As the microwave power increases, this fraction increases until a constant value is reached corresponding to a gas temperature of 3100K. The exact mechanism for this result is difficult to explain with confidence without the use of modelling to point out a significant change in electron temperature or density as the measurements were taken where the N₂ emission was greatest as shown in figure 29. Since electron impact excitation forms the higher lying states for these emissions, the electron impact dissociation could be that of ground state N₂ molecules, meaning at higher microwave powers, the ground state N₂ population is negligible due to a significant amount being dissociated to form NH and excited to the C³Π_u state.

The nitrogen atom flow experiments reveal similar linearly increasing trends for both NH₃ and N₂ that is explained trivially by an increase in mole fraction of N atoms present. The interesting result for these studies is in figure 39, where the gas temperature drops 300K in an N₂ plasma, from 3100K to 2800K over a change of mole fraction from 1% to 6% N₂. However, in the NH₃ plasma the gas temperature remains constant at 3150K. This result must be explained by the amount of N present, due to the measurements being taken at a microwave power of 1.5kW, which is near the point where the gas temperatures are equal for equal N atom flow rates. The temperature in figure 39 must then drop due to a relatively higher ground state N₂ population than for the N atom flow rates used for the microwave power measurements. The ground state atoms are less energetic and therefore more collisions will accompany a decrease in temperature. However, this explanation would need to be verified by computational calculation of the electron energy distribution function as a function of the N atom flow rate in the given precursor gas mixture, microwave power and chamber pressure. It should be noted that any conversion to ionic species such as N₂⁺ during these measurements has a negligible effect on the overall emission, since the ionization degree in the plasma is on the order of 10⁻⁵% [98].

Conclusion

Diamond is a remarkable material, exhibiting many promising mechanical, electronic and thermal properties that see applications in many different areas. Therefore, it is important to understand its structure, thermodynamics and growth processes. MPCVD is a method that produces high quality diamond with similar properties to that found in nature. Therefore, it is of interest to understand the growth process so that optimum films of diamond may be grown with the correct composition of precursor gases and other input parameters. Since the presence of N_2 as a precursor gas was found in the literature to increase the growth rate of diamond, along with no existing literature to the present comparing N_2 and NH_3 plasmas in MPCVD diamond growth, the motivation for this project was born. The project has shown the capability of OES to probe plasma characteristics and the fidelity of PGOPHER, a piece of software developed at the University of Bristol, to simulate experimentally obtained spectroscopic data in order to gain insight into parameters such as the concentrations of important species (like N_2 and NH) and the overall gas temperature. The project showed some interesting results. For example, spatial profile measurements show the N_2 emission is greater in an NH_3/H_2 containing plasma than it is in an N_2/H_2 plasma. Another significant result is the gas temperature remains constant in an NH_3 plasma with variation of the microwave power, whereas with N_2 this was observed to increase. The results presented here do not give any insight into how incorporation of N accelerates the growth process of diamond. However, it is important to understand the gas phase chemistry of N containing gases with H_2 before tackling a system that also incorporates a C containing gas like CH_4 . This is because there are already a staggering amount of reactions that occur in CH_4/H_2 mixtures and to include N to this mix would further complicate analysis. The data provided here should be accompanied by theoretical modelling in order to calculate other parameters in the plasma such as the electron temperature and the electron density for developing an explanation for the results that cannot be explained by OES alone and to confirm the explanations for the results obtained in this study.

Suggestions for further work

Similar measurements to those shown in section 3 were taken for a plasma consisting of N_2 , CH_4 and H_2 source gases. However, the results are not shown because corresponding data with an NH_3 , CH_4 and H_2 plasma were not taken due to the time constraints of this project and therefore the results of the N_2 plasma cannot be compared and contrasted with NH_3 . Whilst the presence of CH_4 adds many dimensions of complication to the reactions that occur in the gas phase, OES may be able to reveal aspects of the plasma that change due to C containing species interacting with N containing species. The NH emission may be expected to reduce to a negligible amount due to the presence of CN that may form under the conditions of MPCVD and act as a getter. The data obtained from these studies should then be computationally modelled like the data shown in the present study to compare and contrast differences in plasma chemistry. The growth rate of diamond in an NH_3 plasma should be recorded and compared with the table given in section 5. This may point towards the use of NH_3 as a precursor gas for increasing the growth rate of diamond. However, in both cases care should be taken as N was shown to be a substitutional defect in section 1. In this case the use of N gas should be treated cautiously when trying to grow a single crystalline sample of diamond for a more specific application than just one that requires its hardness properties.

Measurements should also be taken for MPCVD reactors with precursor gas compositions including inert gases such as Ar. A study in the literature showed that upon addition of 5% Ar to a gas mixture of H_2 , the H Lyman- α line emission increased by an order of magnitude, while the electron temperature for an Ar- H_2 plasma was over a factor of two greater than one consisting of just H_2 [118]. Clearly, this is important given the role that atomic H plays in the plasma as shown in section 1.2.3. Similar measurements to this study should be carried out on various H emission lines in the presence of Ar and without to understand how the H emission varies with microwave power and z.

Acknowledgements

I would like to thank Dr Ben Truscott for his helpful discussions and expert advice both in and out the laboratory. I would also like to thank Dr Colin Western for developing PGOPHER which formed a significant amount of my project work and routinely updating the program during the course of my project. I would also like to thank Professor Mike Ashfold for helpful discussions and support throughout the project.

Finally, I would like to thank everyone in the diamond group at the University of Bristol for their great humour and discussions!

8.

References

- [1] J. D. Bernal, *Proc. R. Soc. Lond. A*, **106**, 750-773 (1924)
- [2] H. Ibach, H. Luth, *Solid-State Physics: An Introduction to Principles of Materials Science*, Fourth Edition, Springer, 35 (2009)
- [3] J. E. Field, *Properties of diamond*, Academic press, London (1993)
- [4] A. L. Ruoff, K. D. Timmerhaus, M. S. Barker, *High Pressure Science and Technology*, Sixth Edition, Plenum, 525-548 (1979)
- [5] A. J. Miller, D. M. Reece, M. D. Hudson, *Dia. Rel. Mat*, **6**, 386-389 (1997)
- [6] M. C. Costello, D. A. Tossell, D. M. Reece, C. J. Brierly, J. A. Savage, *Diam. Rel. Mat*, **6**, 1137-1141 (1994)
- [7] C. A. Rego, P. W. May, E. C. Williamson, M. N. R. Ashfold, Q. S. Chia, K. N. Rosser, N. M. Everitt, *Diam. Rel. Mat*, **3**, 939-941 (1994)
- [8] X. H. Wang, L. Piloni, W. Zhu, W. Yarbrough, W. Drawl, R. Meissier, *J. Mater. Res*, **5**, 2345 (1990)
- [9] C. J. Brierly, C. M. Beck, G. R. Kennedy, J. Metcalfe, D. Wheatley, *Diam. Relat. Mater*, **8**, 1759-1764 (1999)
- [10] C. A. Klein, *Diam. Relat. Mater*, **2**, 1024-1032 (1993)
- [11] M. Allen, F. Law, R. Rushton, *Clin. Mater*, **1**, 1-10 (1994)
- [12] R. Butter, M. Allen, L. Chandra, A. H. Lettington, R. Rushton, *Diam. Relat. Mater*, **4**, 857 (1995)
- [13] D. P Dowling, P. V. Kola, K. Donnelly, *Diam. Relat. Mater*, **6**, 390 (1997)
- [14] R. Hauert, *Diam. Relat. Mater*, **12**, 583-589 (2003)
- [15] A. Grill, *Diam. Relat. Mater*, **12**, 166-170 (2003)
- [16] R. Lappalainen, H. Heinonen, A. Anttila, S. Santavirta, *Diam. Relat. Mater*, **7**, 482-485 (1998)
- [17] J. I. Onate, M. Comin, I. Bracerias, *Surf. Coat. Technol*, **142**, 1056-1062 (2001).
- [18] H. Don't, W. Shi, T. Bell, *Wear*, **1**, 146-153 (1999)
- [19] D. Sheeja, B. K. Tay, X. Shi, *Diam. Relat. Mater*, **10**, 1043-1048 (2001)
- [20] D. G. Onn, A. Witek, Y. Z. Qiu, T. R. Anthony, W. F. Banholzer, *Phys. Rev. Lett*, **68**, 2806-2809 (1992)

- [21] J. R. Olson, R. O. Pohl, J. W. Vandersande, A. Zoltan, T. R. Anthony, W. F. Banholzer, *Phys. Rev. B*, **47**, 14850-14854 (1993)
- [22] J. Callaway, *Phys. Rev.*, **113**, 1046 (1959)
- [23] G. B. Bachelet, G. A. Baraff, M. Schluter, *Phys. Rev. B*, **24**, 4736 (1981)
- [24] S. R. boyd, I. Kiflawi, G. S. Woods, *Philo. Mag. B*, **3**, 351-361 (1995)
- [25] N. Y. Surovtsev, I. N. Kupriyanov, V. K. Malinovsky, V. A. Gusev, Y. N. Pal'yanov, *J. Phys. Condens. Matter*, **11**, 4767-4774 (1999)
- [26] J. Walker, *Rep. Prog. Phys.*, **42**, 1606-1659 (1979)
- [27] K. Iakoubovskii, G. J. Adriaenssens, *Phys. Rev. B*, **61**, 10174 (2000)
- [28] C. D. Clark, H. Kanda, I. Kiflawi, G. Sittas, *Phys. Rev. B*, **51**, 16681 (1995)
- [29] P. H. Chen, C. L. Lin, Y. K. Liu, T. Y. Chung, C. Liu, *IEEE Phot. Tech. Lett.*, **20**, 845 (2008)
- [30] M. S. Eggebert, P. Meissen, F. Schaudel, P. Koidl, A. Vescan, H. Leier, *Diam. Relat. Mater.*, **10**, 744-749 (2001)
- [31] A. V. Sukhadolau, E. V. Ivakin, V. G. Ralchenko, A. V. Khomich, A. V. Vlasov, A. F. Popovich, *Diam. Relat. Mater.*, **14**, 589-593 (2005)
- [32] A. Harkonen, S. Suomalainen, E. Saarinen, L. Orsila, R. Koskinen, O. Okhotnikov, S. Calvez, M. Dawson, *Electr. Lett.*, **42**, 12 (2006)
- [33] W. Saslow, T. K. Bergstresser, M. L. Cohen, *Phys. Rev. Lett.*, **16**, 354-356.
- [34] P. J. Dean, E. C. Lightowers, D. R. Wright, *Phys. Rev.*, **140**, A352 (1965)
- [35] C. D. Clark, P. J. Dean, P. V. Harris, *Proc. Roy. Soc. (London)*, **A277**, 312 (1964)
- [36] C. D. Clark, *J. Phys. Chem. Solids*, **8**, 481 (1959)
- [37] S. A. Kajihara, A. Antonelli, J. Bernhole, *Physica. B*, **185**, 144-149 (1993)
- [38] A. Kraft, *Int. J. Electrochem. Sci.*, **2**, 355-385 (2007)
- [39] R. Kalish, *Diam. Relat. Mater.*, **10**, 1749-1755 (2001)
- [40] L. Rong-Bin, H. Xiao-Jun, S. He-Sheng, H. Xian-Chang, *J. Mat. Sci.*, **59**, 1135-1137 (2004)
- [41] J. Iniesta, P. A. Michaud, M. Panizza, G. Cerisola, A. Aldaz, Ch. Comninellis, *Electrochimica Acta*, **46**, 3573-3578 (2001)
- [42] H. B. Martin, A. Argoitia, U. Landau, A. B. Anderson, J. C. Angus, *J. Electrochem. Soc.*, **143**, L133-L136 (1996)

- [43] A. N. Ndao, F. Zenia, A. Deneuveille, M. Bernard, C. Levy-Clement, *Diam. Relat. Mater*, **9**, 1175-1180 (2000)
- [44] C. Reuben, E. Galun, H. Cohen, R. Tenne, R. Kalish, Y. Muraki, K. Hashimoto, A. Fujishima, J. M. Butler, C. Levy-Clement, *J. Electroanal. Chem*, **396**, 233-239 (1995)
- [45] M. panizza, G. Cerisola, *Electrochimica Acta*, **51**, 191-199 (2005)
- [46] B. V. Sarada, T. N. Rao, D. A. Tryk, A. Fujishima, *Anal. Chem*, **72**, 1632-1638 (2000)
- [47] R. F. Davis, Z. Sitar, B. E. Williams, H. S. Kong, H. J. Kim, J. W. Palmour, J. A. Edmond, J. Ryu, J. T. Glass, C. H. Carter Jr, *Mat. Sci. Eng*, **B1**, 77-104 (1988)
- [48] J. Isberg, J. Hammersberg, E. Johansson, T. Wikstrom, D. J. Twitchen, A. J. Whitehead, S. E. Coe, G. A. Scarsbrook, *Science*, **297**, 1670-1672 (2002)
- [49] M. Kasu, K. Ueda, Y. Yamauchi, A. Tallaire, T. Makimoto, *Diam. Relat. Mater*, **16**, 1010-1015 (2007)
- [50] A. Aleksov, M. Kubovic, N. Kaeb, U. Spitzberg, A. Bergmaier, G. Dollinger, Th. Bauer, M. Schreck, B. Stritzker, E. Kohn, *Diam. Relat. Mater*, **12**, 391-398 (2003)
- [51] T. H. Borst, O. Weis, *Diam. Relat. Mater*, **4**, 948 (1995)
- [52] K. Okano, H. Naruki, Y. Akiba, T. Kurosu, M. Iida, Y. Hirose, T. Nakamura, *J. Appl. Phys*, **28**, 1066 (1989)
- [53] H. Shiomi, Y. Nishibayashi, N. Toda, S. Shikata, *IEEE Electron Device Letters*, **16**, 36 (1995).
- [54] A. Aleksov, A. Vecan, M. Kunze, P. Gluche, W. Ebert, E. Kohn, A. Bergmaier, G. Dollinger, *Diam. Relat. Mater*, **8**, 941 (1999)
- [55] M. Alomari, M. Dipalo, S. Rossi, M-A. Diforte-Poisson, S. Delage, J. F. Carlin N. Grandjean, C. Gaquiere, L. Toh, B. Pecz, E. Kohn, *Diam. Relat. Mater*, **20**, 604-608 (2011)
- [56] J. C. Angus, Y. Wang, M. Sunkara, *Annu. Rev. Mater. Sci*, **21**, 221-248 (1991)
- [57] J. Robertson, *Mater. Sci. Eng*, **37**, 129-281 (2002).
- [58] D. C. Green, D. R. McKenzie, P. B. Lukins, *Mater. Sci. Forum*, **52**, 103 (1990)
- [59] P. J. Fallon, V. S. Veerasamy, C. A. Davis, J. Robertson, G. A. J. Amaratunga, W. I. Milne, *Phys. Rev. B*, **48**, 4777 (1993)
- [60] G. M. Pharr, D. L. Callahan, S. D. McAdams, T. Y. Tsui, S. Anders, A. Anders, J. W. Ager, I. G. Brown, C. S. Bhatia, S. R. P. Silver, J. Robertson, *Appl. Phys. Lett*, **68**, 779 (1996)
- [61] S. Aisenberg, R. Chabot, *J. Appl. Phys*, **42**, 2953 (1971)

- [62] J. Robertson, *Prog. Solid State Chem.* **21**, 199 (1991)
- [63] D. R. McKenzie, *Rep. Prog. Phys.* **59**, 1611 (1996)
- [64] I. I. Aksenov, S. I. Vakula, V. G. Padalka, V. E. Strellnitskii, *Sov. Phys. Tech. Phys.* **25**, 1164 (198)
- [65] F. Davanloo, E. M. Juengerman, D. R. Jander, T. J. Lee, C. B. Collins, *J. Appl. Phys.* **67**, 2081 (1990)
- [66] F. Xiong, Y. Y. Chang, R. P. H. Chang, *Phys. Rev. B*, **48**, 8016 (1993)
- [67] D. L. Pappas, K. L. Saenger, J. Bruley, W. Krakow, J. J. Cuomo, T. Gu, R. W. Collins, *J. Appl. Phys.* **71**, 5675 (1992)
- [68] V. Palshin, E. L. Meletis, S. Ves, S. Logothetidis, *Thin Solid Films*, **270**, 165-172 (1995)
- [69] K. Nassau, J. Nassau, *J. Cryst. Growth*, **46**, 157-172 (1979)
- [70] B. V. Spitsyn, D. B. Derjaguin, *Sci. Am.* **233**, 102-109 (1975)
- [71] R. C. DeVries, *Annu. Rev. Mater. Sci.* **17**, 161-87
- [72] F. P. Bunday, *Physica A*, **156**, 169-178 (1989)
- [73] P. K. Bachmann, *Adv. Mater.* **2**, 195-199 (1990)
- [74] J. C. Angus, H. A. Will, W. S. Stanko, *J. Apply. Phys.* **39**, 2915 (1968)
- [75] B. V. Deryagin, D. V. Fedoseev, V. M. Lukaynovich, B. V. Spitsyn, V. A. Ryanov, V. A. Lavrentyev, *J. Cryst. Growth*, **2**, 380 (1968)
- [76] B. V. Spitsyn, B. V. Deryagin, L. L. Builov, A. A. Klochov, A. E. Gorodetskii, A. V. Smol'yanimov, *Dokl. Akad. Nauk. SSR*, **231**, 333 (1976)
- [77] S. Matsumoto, Y. Sato, M. Kamo, N. Setaka, *Jp. J. Appl. Phys.* **21**, L183-L185 (1982)
- [78] S. Matsumoto, Y. Sato, M. Kamo, N. Setaka, *J. Mater. Sci.* **17**, 3106-3112 (1982)
- [79] Y. Saito, S. Matsuda, S. Nogita, *J. Mater. Sci.* **5**, 565-568 (1986)
- [80] M. Kamo, Y. Sato, S. Matsumoto, N. Setaka, *J. Cryst. Growth*, **62**, 642-644 (1983)
- [81] P. W. May, *Phil. Trans. R. Soc. Lond. A*, **358**, 473-495 (2000)
- [82] H. Matsubara, T. Sakuma, *J. Mat. Sci.* **25**, 4472-4476 (1990)
- [83] J. E. Butler, R. L. Woodin, L. M. Fallon, P. Fallon, *Phil. Trans. R. Soc. Lond. A*, **342**, 15-30 (1993)

- [84] J. C. Angus, A. Argoitia, R. Gat, Z. Li, M. Sunkara, L. Wang, Y. Wang, *Phil. Trans. R. Soc. Lond. A*, **342**, 3-11 (1993)
- [85] H. Rau, F. Picht, *J. Mater. Res*, **7**, 934-949 (1993).
- [86] D. G. Goodwin, *J. Appl. Phys*, **74**, 6895 (1993)
- [87] W. L. Hsu, *J. Appl. Phys*, **72**, 3102 (1992)
- [88] D. G. Goodwin, *J. Appl. Phys*, **74**, 6888-6894 (1993)
- [89] P. K. Tyagi, A. Misra, K. N. Narayanan, P. Rai, M. K. Singh, U. Palnitkar, D. S. Misra, F. Le Normand, M. Roy, S. K. Kulshreshtha, *Diam. Relat. Mater*, **15**, 304-308 (2006)
- [90] R. Ramesham, T. Roppel, R. W. Johnson, J. M. Chang, *Thin Solid Films*, **212**, 96-103 (1992)
- [91] J. M. Hollas, *Modern Spectroscopy*, Fourth Edition, Wiley and sons, 140, (2004)
- [92] D. S. Knight, W. B. White, *J. Mater. Res*, **4**, 384-393, (1989)
- [93] J. Wagner, P. Koidl, C. Koidl, *Appl. Phys. Lett.* **59**, 779 (1991)
- [94] S. Reich, C. Thomsen, *Phil. Trans. R. Soc. Lond. A* **362**, 2271-2288 (2004)
- [95] R. W. Bormett, S. A. Asher, R. E. Witowski, W. D. Partlow, R. Lizewski, F. Pettit, *J. Appl. Phys.* **77**, 5916 (1995)
- [96] Z. Sun, J. R. Shi, B. K. Tay, S. P. Lau, *Diam. Relat. Mater.* **9**, (1979)
- [97] F. Silva, K. Hassouni, X. Bonnin, A. Gicquel, *J. Phys. Condens. Matter*, **21**, 364202-364218 (2009)
- [98] G. J. M. Hagelaar, K. Hassouni, A. Gicquel, *J. Appl. Phys*, **96**, 1819 (2004)
- [99] P. A. Tipler, G. Mosca, *Physics for Scientists and Engineers*, Sixth Edition, W.H. Freeman, 577 (2007)
- [100] J. Amussen, *J. Vac. Sci. Technol. A*, **7**, 883-893 (1989).
- [101] K. Suzuki, S. Okudairo, N. Sadudo, I. Kanomata, *Jpn. J. Appl. Phys*, **16**, 1979 (1977)
- [102] C. Pomot, B. Mahi, B. Petit, Y. Arnal, J. Pelletier, *J. Vac. Sci. Technol. B*, **4**, 1 (1986)
- [103] W. Tan, T. A. Grotjohn, *Diam. Relat. Mater*, **4**, 1145-1154 (1995)
- [104] W. Tan, T. A. Grotjohn, *J. Vac. Sci. Tech. A*, **12**, 1216 (1994)

- [105] M. E. Bojaddaini, H. Chatei, M. Atounti, M. El Haim. I. Driouch, M. El Hammouti, *Adv. Studies Theor. Phys*, **7**, 1071-1085 (2013)
- [106] J. E. Butler, Y. A. Mankelevich, A. Cheesman, J. Ma, M. N. R. Ashfold, *J. Phys. Condens. Matter*, **21**, 364201 (2009)
- [107] G. Lombardi, K. Hassouni, G. D. Stancu, L. Mechold, J. Ropcke, A. Gicquel, *Plasma Sources Sci. Technol.* **14**, 440-450 (2005)
- [108] F. G. Celiii, P. E. Pehrsson, H. T. Wang, J. E. Butler, *Appl. Phys. Lett.* **52** 2043 (1988)
- [109] W. L. Hsu, *Appl. Phys. Lett.* **59**, 1427 (1991)
- [110] G. Z. Cao, J. J. Schermer, W. J. P van Enckevort, W. A. L. M. Elst, L. J. Giling, *J. Appl. Phys*, **79**, 1357 (1996)
- [111] J. Ma, M. N. R. Ashfold, Y. A. Mankelevich, *J. Appl. Phys.* **105**, 043302 (2009)
- [112] J. Ma, A. Cheeseman, M. N. R. Ashfold, K. G. Hay, S. Wright, N. Langford, G. Duxbury, Y. A. Mankelevich, *J. Appl. Phys.* **106**, 03305 (2009).
- [113] R. N. Zare, E. O. Larsson, R. A. Berg, *J. Mol. Spec.* **15**, 117-139 (1965)
- [114] A. Lofthus, P. H. Krupenie, *J. Phys. Chem. Ref. Data*, **6**, 113 (1977)
- [115] C. R. Brazier, R. S. Ram, P. F. Bernath, *J. Mol. Spec.* **120**, 381-402 (1986)
- [116] K. A. Peterson, T. H. Dunning, *J. Phys. Chem*, **95**, 3898-3901 (1995)
- [117] F. G. Bordwell, X. M. Zhang, J. P. Cheng, *J. Org. Chem*, **58**, 6410-6416 (1993)
- [118] R. L. Mills, P. Ray, *New J. Phys.* **4**, 22.1-22.17 (2002)